



universität
wien

MASTERARBEIT

Titel der Masterarbeit

„An acoustic setup for vibration
analysis of silicon wafers“

Verfasser

Stefan Mitterhofer BSc

angestrebter akademischer Grad

Master of Science (MSc)

Wien, 2014

Studienkennzahl lt. Studienblatt:

A 066 876

Studienrichtung lt. Studienblatt:

Masterstudium Physik

Betreuerin / Betreuer:

Ass.-Prof. Dr. Viktor Schlosser

Contents

1	Motivation	1
2	Manufacturing silicon wafers	2
2.1	Crystal growth	2
2.2	Wafer sawing	3
2.3	Polishing and Cleaning	3
3	Theory	5
3.1	The Kirchhoff plate model	5
3.1.1	Thin plate	5
3.1.2	Kirchhoff's hypotheses	5
3.1.3	The biharmonic equation	7
3.1.4	Thin plate vibrations	11
3.2	Finite element analysis of thin plates	13
3.2.1	Modelling the system	14
3.2.2	The element stiffness equations	14
3.2.3	The total potential energy functional	15
3.2.4	The displacement field	16
3.2.5	Stress-strain-displacement relations	17
3.2.6	The global stiffness equation	19
3.2.7	Computer implementation	22
4	Experimental setup	24
4.1	Instruments	26
4.1.1	Accuracy	26
4.1.2	Loudspeaker	27
4.2	Samples	28
4.3	Measurements	30
4.3.1	Variable frequency	30
4.3.2	Variable position	31
4.3.3	Wafer displacements	32
4.4	Laser cutting	33
4.5	Simulation	36
5	Data evaluation	38
5.1	Introduction	38
5.1.1	The frequency spectrum	38
5.1.2	Basic considerations	39
5.1.3	Oscillation patterns and Chladni figures	42

5.2	Variable frequency	46
5.2.1	Microphone signal - voltage	46
5.2.2	Signal power at the loudspeaker	48
5.2.3	Resonance frequency and wafer mass	49
5.3	Variable position	51
5.3.1	Impact of the wafer switching process	51
5.3.2	Impact of cracks	52
5.4	Simulation	54
5.4.1	Resonance frequencies	54
5.4.2	Viability of the Kirchhoff Plate Theory	55
6	Conclusion	56
	References	57
A	Appendix	61
A.1	Symbols	61
A.2	Constants and material properties	63
A.3	Abbreviations	63
A.4	Mesh for the wafer	64
A.5	Table of figures	65
B	Curriculum Vitae	66
C	Abstract - english	67
D	Abstract - german	68

Acknowledgement

I want to thank Ass. Prof. Dr. Viktor Schlosser for his help, guidance and patience during my work, and for suggesting this master thesis.

Furthermore I thank Univ.-Ass. Dr. Johann Summhammer for his help with the laser scribing machine.

Thanks go to my family, especially my mother and my brother, and my friends for their continued support during the past years.

Finally I like to thank Daniel Klotz and Gunther Erhard for proofreading and giving suggestions for improving this work.

1 Motivation

An exponential growth in the installed capacity of photovoltaic power plants has been observed in the last few years. The technology is predicted to become more cost-effective and competitive in the coming years. Therefore a further growth is expected[1].

Crystalline silicon (c-Si) is the most common photovoltaic technology with about 80 % of today's market share[2]. Different stages of the manufacturing process are one source of microcracks and impurities in the wafers. Systems for quality control are therefore increasingly demanded. They should be cost effective, time efficient, accurate, able to be integrated in the manufacturing process and non-destructive. Different methods are in discussion, such as light transmission and scattering, luminescence imaging and bending tests. These methods do not fulfil all the requirements mentioned. Thus new possibilities have to be explored.

Resonant frequencies of c-Si wafers may give informations about their quality: " [...] a dependence of wafer audible mode frequencies on residual stress level that may be useful for solar cell mechanical quality control and breakage inspection" was found[3]. In thin metal plates a fatigue crack leads to a broadening of the second resonance peak[4].

This master thesis investigates the impacts of the wafer's surface cracks on its resonance frequencies and vibrations. Mathematically these wafers can be seen as thin plates, described by the Kirchhoff Plate theory. With finite element analysis the different oscillations are modelled and compared to the experimental results.

2 Manufacturing silicon wafers

To better understand possible sources for cracks and impurities in wafers, in this chapter their manufacturing process is summarized. The process is broadly described in current literature, for example [5] and [6].

2.1 Crystal growth

The most common crystal growth methods are the Czochralski, float-zone and ribbon methods and chemical vapor deposition. Since in my measurements monocrystalline wafers were used, the former two will be described in the following.

For the Czochralski crystal growth, silicon is melted in a graphite crucible. A seed crystal is introduced into the melt, then slowly rotated and pulled out. At the interface to the crystal the melt solidifies. The newly formed solid has the same crystallographic structure as the seed. It is important that the melt cools down very slowly, so that a single-crystal silicon ingot is created at growth rates of about 5 cm/h. Defects and doping nonuniformities can be minimized through control of the temperature gradient within the melt. The dopant can be given directly into the melt. But the melt may be contaminated with other materials, for example the crucible material and impurities in the walls of the crucible. The most common impurities are carbon and oxygen. This effect can be minimized by using magnetic fields to confine the melt.

Another method for manufacturing c-Si wafers is the float-zone method. With radio frequency induction a cylindrical polycrystalline bar is locally melted. The cylinder is then moved through the field, with an average speed of 15 – 30 cm/h. This speed determines the growth rate of the crystal. At one boundary the material melts, at the other it recrystallizes as a single crystal. The dopant can be added into the melted phase.

Since this method does not require contacts between the melted silicon and other materials (as with the crucible in the Czochralski method), impurities can be minimized. Through several passes of the coil inducing the field even higher structural quality and higher purities can be achieved.

In comparison: Float-zone cells have less impurities than Czochralski cells, but have a higher dislocation density and higher cost. The Czochralski method is therefore still the most common crystal growth process.

2.2 Wafer sawing

The main technique for slicing the silicon ingots into wafers is slurry-based multi-wire sawing. It is a costly process which has a big impact on the wafer surface and subsurface.

A steel wire, usually $110\mu\text{m} - 140\mu\text{m}$ in diameter, is wound many times over spools, forming a net of parallel wires. It is coated in a slurry, a suspension of abrasive particles and a carrier fluid. Usually SiC or diamond powders are used as an abrasive, for cost reasons mostly the former. Polyethylene glycol is the most commonly used carrier fluid. The most important roles of the fluid are cooling and lubrication. It transports the abrasive particles, and removes silicon and iron particles worn off from the wire and the ingot.

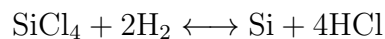
During the sawing process the entire net is moved at the same speed. The silicon ingot is pressed against the net, which cuts it in many wafers. This process causes many micro-cracks on the wafers' surface, see figure 1. These cracks determine the wafer's stability and are one of the main reasons of breakage. Form and density of the cracks depend on the physical properties of the slurry.

2.3 Polishing and Cleaning

After the sawing process the wafers have to be polished. This process is called lapping and consists off pressing a rotating surface against the wafer. Similar to the sawing process a slurry is used, with ultra-fine particles acting as an abrasive. Those particles are much smaller than the ones used in the sawing process and cause less damage to the surface.

Afterwards the wafers are cleaned. Residual slurry, abraded particles and other contaminants affecting the wafer are removed in different chemical baths.

To further increase the quality a thin layer of silicon can be grown on the surface through epitaxial deposition. An example for such a reaction is:



Only Si is solid. The other three substances are gases. In the process the wafer acts as a seed crystal, similar to the seed in the Czochralski crystal growth. Therefore the layer has the same crystallographic orientation.

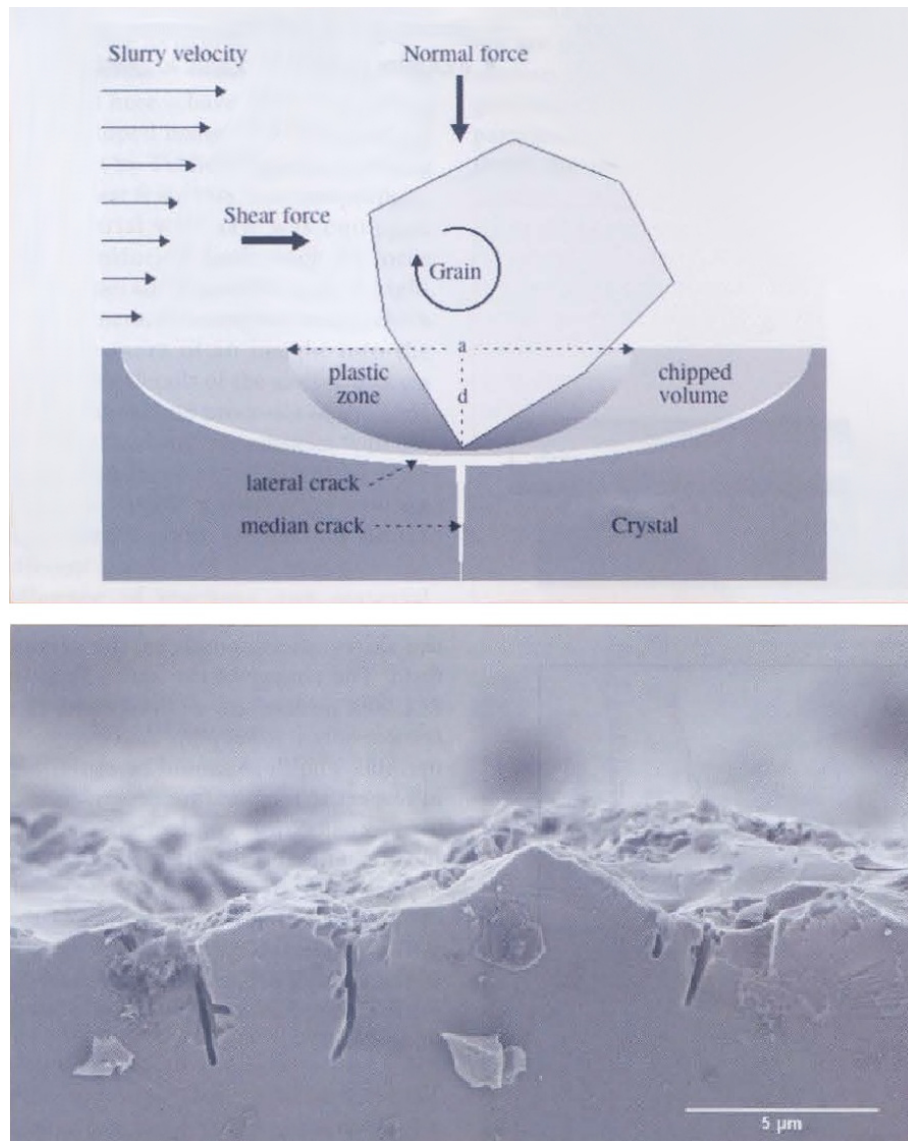


Figure 1: Top: Schematic of an abrasive particle and the acting forces during the sawing process. The median cracks are part of the saw damage. Bottom: The edge of a wafer after the sawing process, imaged with electron microscopy. The roughness of the surface is reduced afterwards, during the polishing process. The deeper cracks remain in the wafer. After [7].

3 Theory

3.1 The Kirchhoff plate model

3.1.1 Thin plate

A plate is a three-dimensional body endowed with special geometric features.:

- *Thinness*: One of the three dimensions of the plate is much smaller than the other two. This dimension is called its thickness h .

Generally the thickness can vary depending on the position, $h = h(x, y)$ (if h points in the direction of z). With a as the length of the plate and b its width:

$$\begin{aligned} h(x, y) &\ll a \\ h(x, y) &\ll b \end{aligned} \tag{1}$$

The ratio a/h (or b/h) determines which theory can be applied. Usually, for thin plates, it is between 8 and 80[9].¹ Plates with a smaller ratio are referred to as thick plates, plates with a higher ratio as membranes. Theories describing plate bending are for example the membrane shell model for membranes, the Kirchhoff model for thin plates and the Reissner-Mindlin model for thin and moderately thick plates.

- *Flatness*: The midsurface of the plate is in its ground state a plane, therefore often referred to as midplane. It is defined as the level in the middle of the thickness of the plate, see figure 2. It may be deformed under load.

3.1.2 Kirchhoff's hypotheses

Kirchhoff's model, sometimes referred to as the classical plate theory, describes the bending of thin plates. It is based on fundamental assumptions, Kirchhoff's hypotheses (here quoted from [9]):

- (A) The material of the plate is elastic, homogeneous and isotropic.
- (B) The plate is initially flat.

¹The exact values vary in literature. They should only give an indication of which theory can best describe a given problem. To choose the most accurate theory its basic assumptions must be considered and compared to the physical problem which has to be analysed.

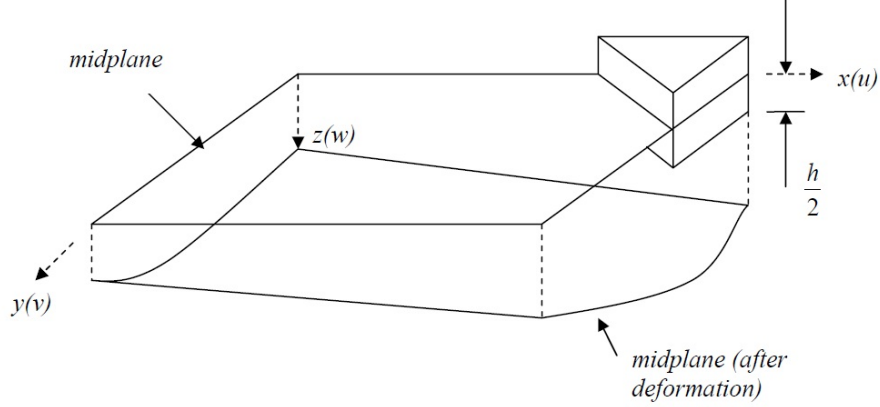


Figure 2: Definition of the midplane. After [9], p.85.

- (C) The deflection of the midplane is small compared with the thickness of the plate. [...]
- (D) The straight lines, initially normal to the middle plane before bending, remain straight and normal to the middle surface during the deformation, and the length of such elements is not altered. [...]
- (E) The stress normal to the middle plane, σ_z is small compared with the other stress components, σ_x and σ_y , and may be neglected in the stress-strain relations.
- (F) Since the displacements of the plate are small, it is assumed that the middle surface remains unstrained after bending.

Some remarks:

- While according to (A) the theory applies only to isotropic materials, it can be extended to anisotropic materials like c-Si. (E) has to be adjusted accordingly: The stresses normal to the middle plane σ_{xz} , σ_{yz} and σ_{zz} are small compared with the other stress components, σ_{xx} , σ_{yy} and σ_{xy} and may be neglected in the stress-strain relations.
- Some of these assumptions directly follow from one another, for example (C),(D) and (A) - homogeneity. Consider two straight lines of particles normal to the midplane in a homogeneous plate. For small deflections the lines are still approximately parallel. Thus the material

is approximately homogeneous. This does not hold true for big deflections compared to the plate's thickness. The material would not be homogeneous in this case. The same considerations can be made for all three assumptions.

3.1.3 The biharmonic equation

Starting from Kirchhoff's hypotheses, in this chapter a derivation for the biharmonic equation based on [8] is outlined. It is the governing equation for plate bending of isotropic plates.

Hooke's law applies to plate bending problems (A). Bending stresses σ_{ii} are linear functions of bending strains e_{ii} , $i = x, y, z$, and vice versa.

$$\begin{bmatrix} \sigma_{xx} \\ \sigma_{yy} \\ \sigma_{xy} \end{bmatrix} = \begin{bmatrix} C_{11} & C_{12} & C_{13} \\ C_{12} & C_{22} & C_{23} \\ C_{13} & C_{23} & C_{33} \end{bmatrix} \begin{bmatrix} e_{xx} \\ e_{yy} \\ 2e_{xy} \end{bmatrix} \quad (2)$$

Note that this only covers two dimensions. The remaining components of the bending stresses are 0 (E). The three-dimensional problem can be reduced to a two-dimensional one, equivalent to the simplifications in the Euler-Bernoulli-beam theory to one dimension.

The bending strains are defined as (after [10]):

$$\begin{aligned} e_{xx} &= \frac{\partial u}{\partial x}, & e_{yy} &= \frac{\partial v}{\partial y}, & e_{zz} &= \frac{\partial w}{\partial z}, & e_{xy} &= \frac{\partial u}{\partial y} + \frac{\partial v}{\partial x} = e_{yx} \\ e_{xz} &= \frac{\partial u}{\partial z} + \frac{\partial w}{\partial x} = e_{zx}, & e_{yz} &= \frac{\partial v}{\partial z} + \frac{\partial w}{\partial y} = e_{zy} \end{aligned} \quad (3)$$

As a result of (D) the displacement $\vec{u} = (u, v, w)$ of any plate particle $P(x, y, z)$ is:

$$u = -z \cdot \frac{\partial w}{\partial x}, \quad v = -z \cdot \frac{\partial w}{\partial y}, \quad w = w \quad (4)$$

Note that z is the distance of the particle to the midplane before the bending

process. With this result we can write equation (3) as:

$$\begin{aligned}
e_{xx} &= -z \cdot \frac{\partial^2 w}{\partial x^2} = -z \cdot \kappa_{xx} \\
e_{yy} &= -z \cdot \frac{\partial^2 w}{\partial y^2} = -z \cdot \kappa_{yy} \\
e_{zz} &= -z \cdot \frac{\partial^2 w}{\partial z^2} = 0 \\
2e_{xy} &= -2z \cdot \frac{\partial^2 w}{\partial x \partial y} = -2z \cdot \kappa_{xy} \\
2e_{xz} &= -\cancel{\frac{\partial w}{\partial x}} + \cancel{\frac{\partial w}{\partial x}} = 0 \\
2e_{yz} &= -\cancel{\frac{\partial w}{\partial y}} + \cancel{\frac{\partial w}{\partial y}} = 0
\end{aligned} \tag{5}$$

The curvatures of the deformed midplane are κ_{ij} .

$$\kappa_{xx} = \frac{\partial^2 w}{\partial x^2}, \quad \kappa_{yy} = \frac{\partial^2 w}{\partial y^2}, \quad \kappa_{xy} = \frac{\partial^2 w}{\partial x \partial y} \tag{6}$$

With κ_{ij} equation (2) can be written as:

$$\begin{bmatrix} \sigma_{xx} \\ \sigma_{yy} \\ \sigma_{xy} \end{bmatrix} = -z \cdot \begin{bmatrix} C_{11} & C_{12} & C_{13} \\ C_{12} & C_{22} & C_{23} \\ C_{13} & C_{23} & C_{33} \end{bmatrix} \begin{bmatrix} \kappa_{xx} \\ \kappa_{yy} \\ 2\kappa_{xy} \end{bmatrix} \tag{7}$$

The bending stress from the deflection results in bending moments M_{xx} and M_{yy} and the twisting moment M_{xy} . They can be calculated by analysing a cuboid $dx \cdot dy \cdot h$ of the plate (see figure 3).

$$\begin{aligned}
M_{xx} dy &= \int_{-h/2}^{h/2} -\sigma_{xx} z \cdot dz \cdot dy \\
\Rightarrow M_{xx} &= \int_{-h/2}^{h/2} -\sigma_{xx} z \cdot dz \\
&= - \int_{-h/2}^{h/2} [-z \cdot (C_{11}\kappa_{xx} + C_{12}\kappa_{yy} + 2C_{13}\kappa_{xy}) \cdot z] dz \\
&= \frac{z^3}{3} \cdot (C_{11}\kappa_{xx} + C_{12}\kappa_{yy} + 2C_{13}\kappa_{xy}) \Big|_{-h/2}^{h/2} \\
&= \frac{h^3}{12} (C_{11}\kappa_{xx} + C_{12}\kappa_{yy} + 2C_{13}\kappa_{xy})
\end{aligned} \tag{8}$$

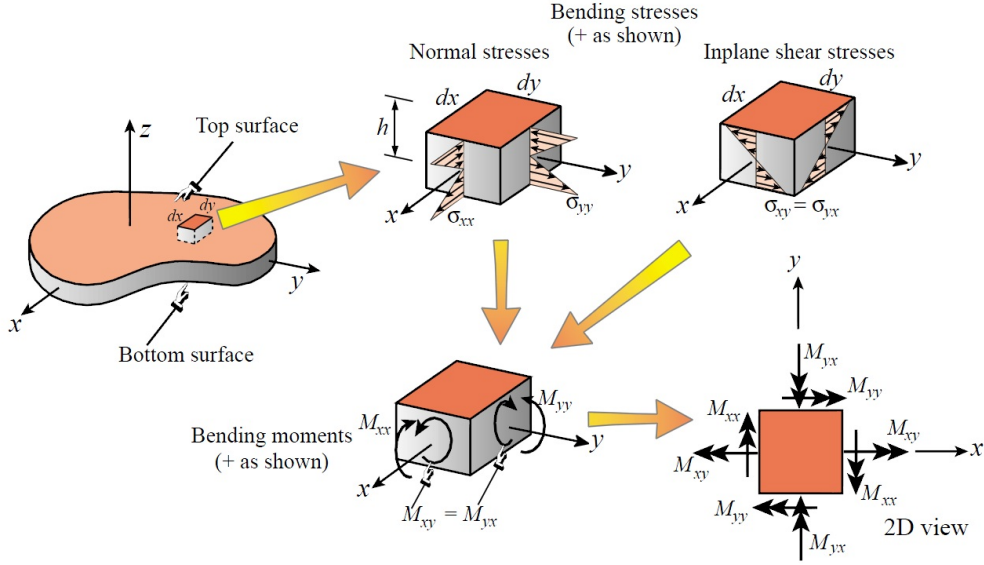


Figure 3: Bending stresses and moments. After [8], p. 26-8.

The moments M_{yy} and M_{xy} can be calculated analogously. Inserting the results into equation (7) yields:

$$\begin{bmatrix} M_{xx} \\ M_{yy} \\ M_{xy} \end{bmatrix} = \frac{h^3}{12} \cdot \begin{bmatrix} C_{11} & C_{12} & C_{13} \\ C_{12} & C_{22} & C_{23} \\ C_{13} & C_{23} & C_{33} \end{bmatrix} \begin{bmatrix} \kappa_{xx} \\ \kappa_{yy} \\ 2\kappa_{xy} \end{bmatrix} = \begin{bmatrix} D_{11} & D_{12} & D_{13} \\ D_{12} & D_{22} & D_{23} \\ D_{13} & D_{23} & D_{33} \end{bmatrix} \begin{bmatrix} \kappa_{xx} \\ \kappa_{yy} \\ 2\kappa_{xy} \end{bmatrix} \quad (9)$$

Thereby D_{ij} denotes the flexural rigidity or plate rigidity coefficient.

$$D_{ij} = C_{ij} \cdot \frac{h^3}{12} \quad (10)$$

For a further analysis the equilibrium equations of the plate have to be considered. The third component q of the applied lateral force per unit area \vec{q} in equilibrium is:

$$q = - \left(\frac{\partial Q_x}{\partial x} + \frac{\partial Q_y}{\partial y} \right) \quad (11)$$

with the other two components being 0. (Q_x, Q_y) are the components of a transverse shear force.² From moment equilibrium about x and y follows:

$$\frac{\partial M_{xx}}{\partial x} + \frac{\partial M_{xy}}{\partial y} = -Q_y, \quad \frac{\partial M_{yx}}{\partial x} + \frac{\partial M_{yy}}{\partial y} = -Q_x \quad (12)$$

²One of the inconsistencies of the Kirchhoff plate theory emerges: Transverse shear forces are required to describe the equilibrium, but after (E) $\sigma_{xz} = \sigma_{yz} = 0$, as a result there are no such forces.

Equation (12) and equation (13) yield:

$$\frac{\partial^2 M_{xx}}{\partial x^2} + 2 \cdot \frac{\partial^2 M_{xy}}{\partial x \partial y} + \frac{\partial^2 M_{yy}}{\partial y^2} = q \quad (13)$$

By inserting the bending moments from equation (9) it is possible to bring the force along the z direction in relation to the curvature of the plate and therefore with its deflection.

$$\begin{aligned} q &= \frac{\partial^2 (D_{11}\kappa_{xx} + D_{12}\kappa_{yy} + 2D_{13}\kappa_{xy})}{\partial x^2} + 2 \cdot \frac{\partial^2 (D_{12}\kappa_{xx} + D_{22}\kappa_{yy} + 2D_{23}\kappa_{xy})}{\partial x \partial y} \\ &\quad + \frac{\partial^2 (D_{13}\kappa_{xx} + D_{23}\kappa_{yy} + 2D_{33}\kappa_{xy})}{\partial y^2} \\ &= D_{11} \frac{\partial^4 w}{\partial x^4} + D_{12} \frac{\partial^4 w}{\partial x^2 \partial y^2} + 2D_{13} \frac{\partial^4 w}{\partial x^3 \partial y} + 2 \left(D_{12} \frac{\partial^4 w}{\partial x^3 \partial y} + D_{22} \frac{\partial^4 w}{\partial x \partial y^3} \right. \\ &\quad \left. + 2D_{23} \frac{\partial^4 w}{\partial x^2 \partial y^2} \right) + D_{13} \frac{\partial^4 w}{\partial x^2 \partial y^2} + D_{23} \frac{\partial^4 w}{\partial y^4} + 2D_{33} \frac{\partial^4 w}{\partial x \partial y^3} \\ &= D_{11} \frac{\partial^4 w}{\partial x^4} + (2D_{13} + 4D_{12}) \frac{\partial^4 w}{\partial x^3 \partial y} + (D_{12} + 2D_{23} + D_{13}) \frac{\partial^4 w}{\partial x^2 \partial y^2} \\ &\quad + (2D_{22} + 2D_{33}) \frac{\partial^4 w}{\partial x \partial y^3} + D_{23} \frac{\partial^4 w}{\partial y^4} \end{aligned} \quad (14)$$

For a homogeneous, isotropic plate the flexural rigidity is:

$$D = \frac{Eh^3}{1 - \nu^2} \quad (15)$$

Here E denotes the elastic modulus and ν the Poisson ratio. Equation (14) is in this special case the biharmonic equation:

$$\boxed{D \cdot \nabla^4 w = D \nabla^2 \nabla^2 w = q} \quad (16)$$

The biharmonic operator ∇^4 is defined as:

$$\nabla^4 \equiv \frac{\partial^4}{\partial x^4} + 2 \cdot \frac{\partial^4}{\partial x^2 \partial y^2} + \frac{\partial^4}{\partial y^4} \quad (17)$$

The force per unit area \vec{q} can be written as $\vec{q} \cdot A = d\vec{p}/dt$, where A is a normalized area. The mass is constant.

$$\vec{q} = (0, 0, q) = \frac{m}{A} \cdot \frac{d^2(u, v, w)}{dt^2} \quad (18)$$

Consider a cuboid in the plate with height h , base area A and density ρ . Its mass is

$$m = \rho h A \quad (19)$$

With the equations (18) and (19) the biharmonic equation can be written in its more common form:

$$\boxed{D \cdot \nabla^4 w(x, y, t) = q = \rho h \cdot \frac{\partial^2 w(x, y, t)}{\partial t^2}} \quad (20)$$

Remark: All partial differential equations of the form (20) are referred to as biharmonic equations. For example the homogeneous, time-independent biharmonic equation is, with an arbitrary function $\Phi = \Phi(x, y)$:

$$\nabla^4 \Phi = 0 \quad (21)$$

3.1.4 Thin plate vibrations

Resonances of thin plates have been studied and described by E.Chladni[11]. In his experiments a plate was clamped in its center. It was lightly covered with sand. A violin bow was drawn over the plate, which began to vibrate in one of its eigenfrequencies. The sand accumulated in the nodal lines of the eigenmodes. The visible sand patterns on the plate are called Chladni patterns.³

For calculating the eigenfrequencies the biharmonic equation has to be solved. Because plate bending and plate vibrations are commonly encountered in engineering, it has been thoroughly analysed and analytically solved for simple geometries and different boundary conditions. Two examples of different approaches are outlined in the following.

Wave approach: [13] An ansatz for the solution of the biharmonic equation is made using separation of variables:

$$\begin{aligned} w(x, y, t) &= w(x) \cdot w(y) \cdot \exp(i\omega t) \\ &= x_0 \cdot y_0 \cdot \exp(-ik_1 x) \cdot \exp(ik_2 y) \cdot \exp(i\omega t) \end{aligned} \quad (22)$$

³Chladni patterns show the nodal lines and areas where the amplitude of the oscillation is biggest. This was described by M.Faraday[12]: Very small particles are thrown from the vibrating plate into the air and caught in the air current above. The current transports them to areas where the oscillation amplitude is greatest. The particles in Chladni's experiments were shavings from the hairs of the violin bow.

The wave numbers are k_1 and k_2 , x_0 and y_0 are arbitrary constants and ω is the frequency. Substituting (22) in (20) and rewriting yields:

$$\omega = (k_1^2 + k_2^2) \sqrt{\frac{D}{\rho h}} \quad (23)$$

With the boundary conditions the propagation and reflection matrices can be derived. With those the relations between incident and reflected waves at the two opposite boundaries can be described. The solutions of the obtained linear equation system can be used to calculate the wave numbers. For two opposite edges simply supported and the other two free they are, with a and b as length and width of the plate:

$$\begin{aligned} k_1 &= \frac{n\pi}{a}, \quad n = 1, 2, \dots \\ k_2 &= \frac{m\pi}{b}, \quad m = 1, 2, \dots \end{aligned} \quad (24)$$

Substituting yields:

$$\omega_{nm} = \pi^2 \left(\frac{n^2}{a^2} + \frac{m^2}{b^2} \right) \sqrt{\frac{D}{\rho h}}, \quad n, m = 1, 2, \dots \quad (25)$$

Principle of least action: [14] The flexural vibrations of a rectangular cantilever (1 edge clamped, 3 edges free) are analysed. Therefore the solution of the biharmonic equation must be symmetric about the x axis (which is normal to the clamped edge). This holds true only for even functions of y .

$$\begin{aligned} w(x, y, t) &= \sum_{n=0}^N w_{2n}(x, t) \cdot y^{2n} \\ &\approx w_0(x, t) + y^2 w_2(x, t) \end{aligned} \quad (26)$$

Then the action integral \mathcal{A} is formulated with the Lagrangian L , the kinetic energy E_{kin} and the potential energy E_{pot} .

$$\mathcal{A} = \int_0^T L dt = \int_0^T E_{kin} - E_{pot} dt \quad (27)$$

By using the calculus of variation the conditions for w_0 and w_2 for minimizing \mathcal{A} are determined. The equations are simplified by introducing the scaled variables:

$$\hat{x} = \frac{x}{L}, \quad \hat{y} = \frac{y}{L}, \quad \hat{t} = \sqrt{\frac{D}{h\rho}} \cdot \frac{t}{L^2}, \quad \hat{w}_0 = w_0, \quad \hat{w}_2 = a^2 w_2 \quad (28)$$

The length of the cantilever is a . The solutions of the equation have to satisfy:

$$\hat{w}_0(\hat{x}, \hat{t}) = f(\hat{x}) \exp(ikt), \quad \hat{w}_2(\hat{x}, \hat{t}) = g(\hat{x}) \exp(ikt) \quad (29)$$

The scaled frequency parameter is denoted k . The eigenfrequencies of the flexural vibrations of the cantilever are:

$$\omega = k \frac{h}{a^2} \sqrt{\frac{E}{12(1 - \nu^2)\rho}} \quad (30)$$

To obtain an expression for k the reduced governing equations have to be solved. This is done using a singular perturbation analysis, which after lengthy calculations yields an asymptotic solution.

As seen in these two examples, even for simple geometries as rectangular plates exact analytical solutions for some boundary conditions are difficult to obtain. Only several boundary conditions allow for an evaluation leading to an exact solution. Thus for plate bending and vibration approximate methods, as the variational approach described in the second example, have to be used. "The most efficient and well-accepted method at the present time - the finite element method -" is one possibility to obtain such approximate solutions[15].

3.2 Finite element analysis of thin plates

The basic concept of finite element analysis (FEA) is dividing the system into single small elements. They have to be small enough to be described reasonably well by simple mathematical models. These models can then be extended to the whole system, while taking into account the interaction between the single elements.

There are different possibilities to solve the equations, which describe the problem at hand. The most common method in FEA, also applicable to plate bending, is the direct stiffness method (DSM). It was first introduced to FEA by [17]. In the following the basic steps to simulate a given problem using DSM are shown, using thin plate bending as an example; based on the information given in [18].

3.2.1 Modelling the system

The first step is creating a model equivalent to the physical system, i.e. the plate. It is created as a polygon mesh consisting of *elements*. They are connected at points called *nodes*.

The mesh is 2-dimensional with information about length, width and form of the plate and the number of elements. Figure 4 depicts the mesh, which is used to model the wafer.

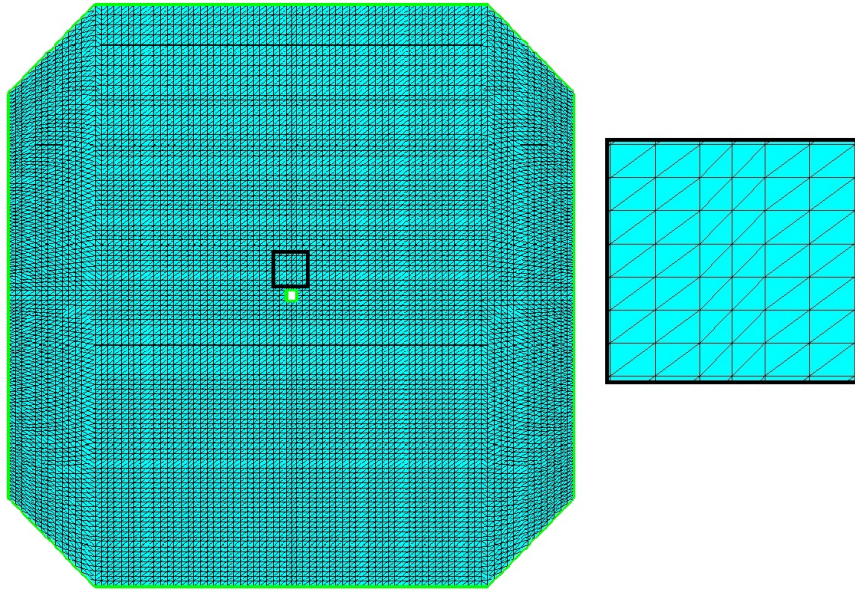


Figure 4: Left: The mesh used to model the wafer with 10000 polygons, in this case triangles. It was created with ElmerGrid[16]. The file can be found in Appendix A.4. Right: The boxed area on the wafer is magnified to show the triangles.

3.2.2 The element stiffness equations

In order to use DSM the model has to be disassembled into single elements and their nodes. Triangular elements, as used in this thesis, need at least three nodes to describe their geometry. They are usually set in the element's corners. In that case the triangle, with its nodes, is called *Turner triangle*[19]. To each element a Cartesian coordinate system (CS) $(\bar{x}^{(e)}, \bar{y}^{(e)}, \bar{z}^{(e)})$, $e = 1, 2, \dots, m$, is assigned, which is called element CS. (e) is an identifier for the element, m is the number of elements. The CS (x, y, z) is called global CS.

In the chapters 3.2.2 - 3.2.5 all properties for single elements and nodes are described in the corresponding element CS.

The forces \vec{F} and displacements \vec{d} are analysed. \vec{F} and \vec{d} are vectors with $3n_e$ components, n_e being the number of nodes per element.

$$\vec{F} = \begin{bmatrix} f_{x1} \\ f_{y1} \\ f_{z1} \\ f_{x2} \\ \vdots \\ f_{zn_e} \end{bmatrix}, \quad \vec{d} = \begin{bmatrix} d_{x1} \\ d_{y1} \\ d_{z1} \\ d_{x2} \\ \vdots \\ d_{zn_e} \end{bmatrix} \quad (31)$$

The component f_{ij} of the force in the direction of $i = x, y, z$ is acting on node $j = 1, 2, \dots, n_e$. The resulting displacement of node $j = 1, 2, \dots, n_e$ in the direction of $i = x, y, z$ is denoted d_{ij} .⁴ The displacements are the primary unknowns. Because of their physical interpretation they are called *degrees of freedom*.

The element stiffness equations relate \vec{F} and \vec{d} .

$$\begin{bmatrix} f_{x1} \\ f_{y1} \\ \vdots \\ f_{zn_e} \end{bmatrix} = \begin{bmatrix} S_{x1x1} & S_{x1y1} & \cdots & S_{x1zn_e} \\ S_{y1x1} & S_{y1y1} & \cdots & S_{y1zn_e} \\ \vdots & \vdots & \ddots & \vdots \\ S_{zn_ex1} & S_{zn_ey1} & \cdots & S_{zn_ezn_e} \end{bmatrix} \begin{bmatrix} d_{x1} \\ d_{y1} \\ \vdots \\ d_{zn_e} \end{bmatrix} \quad (32)$$

$$\boxed{\vec{F} = \mathbf{S} \cdot \vec{d}} \quad (33)$$

The matrix \mathbf{S} is called local stiffness matrix.

3.2.3 The total potential energy functional

The calculation of \mathbf{S} and \vec{F} requires the total potential energy functional Π .

$$\Pi = E_{int} + V \quad (34)$$

The internal energy E_{int} is the elastic strain energy. The potential V results from the applied forces, which are distributed loads and boundary forces.

It is possible to derive the stiffness equations by defining:

$$E_{int} \equiv \frac{1}{2} \vec{d}^T \mathbf{S} \vec{d} \quad (35)$$

⁴Note that \vec{d} and its components d_{ij} are different from \vec{u} and its components (u, v, w) . \vec{u} describes the displacement for all points of the plate $\vec{u}(x, y)$. \vec{d} only describes displacements of the nodes. Their relation is looked at in chapter 3.2.4

$$V \equiv -\vec{d}^T \vec{F} \quad (36)$$

After [20] is E_{int} in an element:

$$\begin{aligned} E_{int} &= \int_{h \cdot \Omega^\circ} \frac{1}{2} C_{ijkl} e_{ij} e_{kl} d(h \cdot \Omega^\circ) \\ &= \frac{1}{2} \int_{\Omega^\circ} h \sigma_{kl} e_{kl} d\Omega^\circ \\ &= \frac{1}{2} \int_{\Omega^\circ} h \vec{\sigma}^T \vec{e} d\Omega^\circ \end{aligned} \quad (37)$$

Thereby h is the element's thickness, Ω° its ground area, $h \cdot \Omega^\circ$ its volume. For the calculation of V boundary conditions are required. They can be given for the displacement \vec{u} or for the stress $\vec{\sigma}$. Former are discarded for now. They are not needed until the last steps of the DSM. Latter are also called force boundary conditions, because they describe the force per unit area acting on a boundary. With $\vec{\sigma}_0$ as a prescribed force, acting on the boundary Γ° of the plate, V is:

$$V = - \int_{\Omega^\circ} h \vec{u}^T \vec{b} d\Omega^\circ - \int_{\Gamma^\circ} h \vec{u}^T \vec{\sigma}_0 d\Gamma^\circ \quad (38)$$

The first addend of this equation describes the potential from the body forces \vec{b} , the second from the boundary forces. \vec{b} are forces acting on a volume of the plate, thus sometimes called volume forces or distributed load. An example is the plate's weight.

With equations (35) and (37) expressions for the stiffness matrix \mathbf{S} can be found. Analogously with equations (36) and (38) the forces on the nodes F can be calculated. Because the stiffness equations relate \mathbf{S} , \vec{F} and \vec{d} , the terms in the equations (37) and (38) have to be expressed in dependence of \vec{d} .

3.2.4 The displacement field

Introduced in equation (31), \vec{d} are the displacements of the nodes. Thus, the local stiffness equations only describe the forces and displacements for the nodes, not for an entire element. But \vec{d} can be interpolated over the whole element to the displacement field $\vec{u} = (u, v, w)$, which components are given

by equation (4). The interpolation is, with the element shape functions N_i :

$$\begin{aligned} u &= \sum_{i=1}^{n_e} N_i(x, y) d_{xi} \\ v &= \sum_{i=1}^{n_e} N_i(x, y) d_{yi} \\ w &= \sum_{i=1}^{n_e} N_i(x, y) d_{zi} \end{aligned} \quad (39)$$

In matrix form equation (39) is:

$$\begin{bmatrix} u \\ v \\ w \end{bmatrix} = \begin{bmatrix} N_1 & 0 & 0 & N_2 & 0 & 0 & \dots & N_{n_e} & 0 & 0 \\ 0 & N_1 & 0 & 0 & N_2 & 0 & \dots & 0 & N_{n_e} & 0 \\ 0 & 0 & N_1 & 0 & 0 & N_2 & \dots & 0 & 0 & N_{n_e} \end{bmatrix} \vec{d} \quad (40)$$

$$\vec{u} = \mathbf{N} \vec{d} \quad (41)$$

The matrix \mathbf{N} is the shape function matrix.

Note that $N_i \stackrel{!}{=} 1$ and $N_{j \neq i} \stackrel{!}{=} 0$ at node i . This means, that the displacement field \vec{u} at node i must be equal to the displacements (d_{xi}, d_{yi}, d_{zi}) .

3.2.5 Stress-strain-displacement relations

The relation between $\vec{\epsilon}$ and $\vec{\sigma}$ for the whole plate in the global coordinate system is described by equation (2). It holds also true for single elements in the corresponding element CS. In compact matrix form this is:

$$\vec{\sigma} = \mathbf{C} \vec{\epsilon} \quad (42)$$

The equations in (3) relate \vec{u} and $\vec{\epsilon}$. They hold true for single elements in their element CS, too. They can be combined in one equation:⁵

$$\begin{bmatrix} e_{xx} \\ e_{yy} \\ 2e_{xy} \end{bmatrix} = \begin{bmatrix} \partial/\partial x & 0 & 0 \\ 0 & \partial/\partial y & 0 \\ \partial/\partial y & \partial/\partial x & 0 \end{bmatrix} \begin{bmatrix} u \\ v \\ w \end{bmatrix} \quad (43)$$

This 3×3 matrix is denoted \mathbf{P} . Note that in 3 dimensions it would be a 6×3 matrix, but it can be simplified because of the considerations in chapter 3.1. In compact matrix form the equation can be written as:

$$\vec{\epsilon} = \mathbf{P} \vec{u} \quad (44)$$

⁵Remember: The coordinates (x, y, z) do represent $(\bar{x}^{(e)}, \bar{y}^{(e)}, \bar{z}^{(e)})$, because single elements and nodes are described.

Inserting equation (44) into equation (41) yields a relation between the strains in an element \vec{e} and the displacements at the nodes \vec{d} :

$$\vec{e} = \begin{bmatrix} \frac{\partial N_1}{\partial x} & 0 & 0 & \frac{\partial N_2}{\partial x} & 0 & \dots & \frac{\partial N_{ne}}{\partial x} & 0 & 0 \\ 0 & \frac{\partial N_1}{\partial y} & 0 & 0 & \frac{\partial N_2}{\partial y} & \dots & 0 & \frac{\partial N_{ne}}{\partial y} & 0 \\ \frac{\partial N_1}{\partial y} & \frac{\partial N_1}{\partial x} & 0 & \frac{\partial N_2}{\partial y} & \frac{\partial N_2}{\partial x} & \dots & \frac{\partial N_{ne}}{\partial y} & \frac{\partial N_{ne}}{\partial x} & 0 \end{bmatrix} \vec{d} = \mathbf{B} \vec{d} \quad (45)$$

The matrix \mathbf{B} is the strain-displacement matrix.

$$\mathbf{B} = \mathbf{P} \mathbf{N} \quad (46)$$

The relations between $\vec{\sigma}$ and \vec{d} are given by:

$$\begin{bmatrix} \partial/\partial x & 0 & \partial/\partial y \\ 0 & \partial/\partial y & \partial/\partial x \\ 0 & 0 & 0 \end{bmatrix} \begin{bmatrix} \sigma_{xx} \\ \sigma_{yy} \\ \sigma_{xy} \end{bmatrix} = - \begin{bmatrix} b_x \\ b_y \\ b_z \end{bmatrix} \quad (47)$$

$$\mathbf{P}^T \vec{\sigma} = -\vec{b} \quad (48)$$

The body forces are $\vec{b} = -\mathbf{P}^T \mathbf{C}(\mathbf{P} \vec{u}) = -\mathbf{P}^T \mathbf{C} \mathbf{B} \vec{d}$ (see [18]).

Now the elastic strain energy $E_{int}(\vec{d})$ can be expressed:

$$E_{int} = \frac{1}{2} \int_{\Omega^\circ} h \vec{\sigma}^T \vec{e} \, d\Omega^\circ = \frac{1}{2} \int_{\Omega^\circ} h \vec{d}^T \mathbf{B}^T \mathbf{C} \mathbf{B} \vec{d} \, d\Omega^\circ \quad (49)$$

Comparing the equations (49) and (35) yields for the element stiffness matrix:

$$\boxed{\mathbf{S} = \int_{\Omega^\circ} h \mathbf{B}^T \mathbf{C} \mathbf{B} \, d\Omega^\circ} \quad (50)$$

Analogously the potential $V(\vec{d})$ can be written:

$$\begin{aligned} V &= - \int_{\Omega^\circ} h \vec{u}^T \vec{b} \, d\Omega^\circ - \int_{\Gamma^\circ} h \vec{u}^T \vec{\sigma}_0 \, d\Gamma^\circ \\ &= - \int_{\Omega^\circ} h \vec{d}^T \mathbf{N}^T \vec{b} \, d\Omega^\circ - \int_{\Gamma^\circ} h \vec{d}^T \mathbf{N}^T \vec{\sigma}_0 \, d\Gamma^\circ \end{aligned} \quad (51)$$

Comparing the equations (51) and (36) yields for the force acting on the node:

$$\boxed{\vec{F} = \int_{\Omega^\circ} h \mathbf{N}^T \vec{b} \, d\Omega^\circ + \int_{\Gamma^\circ} h \mathbf{N}^T \vec{\sigma}_0 \, d\Gamma^\circ} \quad (52)$$

3.2.6 The global stiffness equation

The solutions for the single elements can be merged. The first step in doing so is to express the element stiffness equations in the global CS (x, y, z) . To distinguish between values in the global CS and in the element CS, latter will be marked with a bar over their symbol, e.g. \bar{f}_{ij} . To differentiate between values for the whole plate and values for single elements, latter will be marked with $^\circ$, e.g. f_{ij}° . The superscript $^\circ$ can be seen as an identifier for the element: $^\circ = (1), (2), \dots, (m)$, where m is the number of elements. The brackets are supposed to distinguish it from an exponent.

Transformation matrices, which describe a change of basis, connect $\bar{\vec{F}}$ and $\bar{\vec{d}}$ to \vec{F} and \vec{d} . \mathbf{T}_f° denotes the force transformation matrix, \mathbf{T}_d° the displacement transformation matrix.

$$\vec{F}^\circ = \mathbf{T}_f^\circ \bar{\vec{F}}, \quad \bar{\vec{d}}^\circ = \mathbf{T}_d^\circ \vec{d}^\circ \quad (53)$$

Remark: Note that the force in the element CS is on the right side of its equation, the displacement in the element CS on the left side of its equation. The reason is: \vec{d} is a vector with contravariant components. \vec{F} is a dual vector with covariant components. They change accordingly under basis transformations.

\mathbf{T}_f° is the transpose of \mathbf{T}_d° [18]. Thus we set $\mathbf{T}_d^\circ \equiv \mathbf{T}^\circ$ and $\mathbf{T}_f^\circ \equiv (\mathbf{T}^\circ)^T$. Equation (53) can be written as:

$$\vec{F}^\circ = (\mathbf{T}^\circ)^T \bar{\vec{F}}, \quad \bar{\vec{d}}^\circ = \mathbf{T}^\circ \vec{d}^\circ \quad (54)$$

An example of a basis transformation is shown in figure 5. $(\mathbf{T}^\circ)^T$ follows from simple geometric considerations.

$$\begin{bmatrix} f_{x1}^\circ \\ f_{y1}^\circ \\ f_{z1}^\circ \\ \vdots \\ f_{xn_e}^\circ \\ f_{yn_e}^\circ \\ f_{zn_e}^\circ \end{bmatrix} = \begin{bmatrix} \begin{pmatrix} c^\circ & -s^\circ & 0 \\ s^\circ & c^\circ & 0 \\ 0 & 0 & 1 \end{pmatrix} & \dots & \mathbf{0} \\ \vdots & \ddots & \vdots \\ \mathbf{0} & \dots & \begin{pmatrix} c^\circ & -s^\circ & 0 \\ s^\circ & c^\circ & 0 \\ 0 & 0 & 1 \end{pmatrix} \end{bmatrix} \begin{bmatrix} \bar{f}_{x1}^\circ \\ \bar{f}_{y1}^\circ \\ \bar{f}_{z1}^\circ \\ \vdots \\ \bar{f}_{xn_e}^\circ \\ \bar{f}_{yn_e}^\circ \\ \bar{f}_{zn_e}^\circ \end{bmatrix} \quad (55)$$

Here $c^\circ = \cos \varphi^\circ$ and $s^\circ = \sin \varphi^\circ$ describe a rotation.

From analogous considerations follows \mathbf{T}° . In this special case, the basis is orthogonal and only a rotation of the axes is described. Thus the inverse $(\mathbf{T}^\circ)^{-1}$ is equal to the transpose $(\mathbf{T}^\circ)^T$, and equation (54) can be written as:

$$\bar{\vec{F}}^\circ = \mathbf{T}^\circ \vec{F}^\circ, \quad \bar{\vec{d}}^\circ = \mathbf{T}^\circ \vec{d}^\circ \quad (56)$$

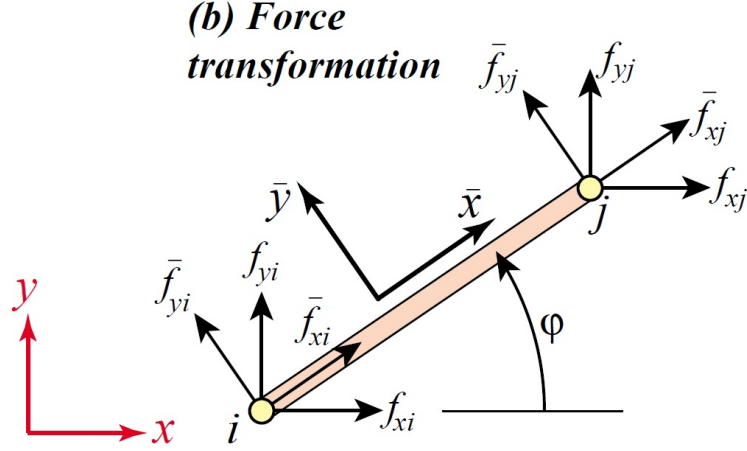


Figure 5: Force transformations between an element CS and the global CS for a simple system of 2 nodes. The direction of z is normal to the plane of projection. After [18], p. 2-13.

This can not be extended to a more general case. In the following therefore equation (54) will be taken for describing the coordinate transformation.

With the element stiffness equations in the global CS and in the element CS, and with equation (54), the correlation between the stiffness matrices in the global CS and in the element CS can be given.

$$\begin{aligned}
 \mathbf{S}^\circ \vec{u}^\circ &= \vec{F}^\circ \\
 &= (\mathbf{T}^\circ)^T \vec{\bar{F}}^\circ \\
 &= (\mathbf{T}^\circ)^T \bar{\mathbf{S}}^\circ \vec{u}^\circ \\
 &= (\mathbf{T}^\circ)^T \bar{\mathbf{S}}^\circ \mathbf{T}^\circ \vec{u}^\circ
 \end{aligned} \tag{57}$$

$$\Rightarrow \boxed{\mathbf{S}^\circ = (\mathbf{T}^\circ)^T \bar{\mathbf{S}}^\circ \mathbf{T}^\circ} \tag{58}$$

Now that all element stiffness equations are given in the global CS, they can be connected again. Two rules apply:

- *Compatibility of displacements:* All elements connecting at a node have the same displacements \vec{d}_{ij}° .

$$\vec{d}_{ij}^\circ = \vec{d}_{ij}^\bullet, \quad \circ, \bullet = (1), (2), \dots, (m), \quad i = x, y, z, \quad j = 1, 2, \dots, n_s \tag{59}$$

The number of the elements is m , the number of nodes in the whole system n_s .

- *Force equilibrium:* The external force F_{ij} at a node is equal to the sum of the internal forces F_{ij}° .

$$F_{ij} = \sum_{\circ=(1)}^{(m)} F_{ij}^\circ, \quad i = x, y, z, \quad j = 1, 2, \dots, n_s \quad (60)$$

The first rule allows dropping the identifier for the element \circ at the displacements. Thus now the global stiffness equation can be written. Analogously to its counterpart for single elements, it relates the force \vec{F} acting on a node to its displacement \vec{d} . \mathbf{S} is the global stiffness matrix.

$$\boxed{\vec{F} = \sum_{\circ} \vec{F}^\circ = \left(\sum_{\circ} \mathbf{S}^\circ \right) \vec{d} = \mathbf{S} \vec{d}} \quad (61)$$

Note that in this method the element stiffness matrices have to be expanded from $n_e \times n_e$ to $n_s \times n_s$ matrices. This yields $n_s \cdot n_s \cdot m$ matrix entries. Because single elements are only connected with a few nodes, in large systems most components of these matrices are 0. This is called a sparse linear system. Since sparse matrices represent a waste of storage, computer-oriented methods differ as described in chapter 3.2.7.

The last step is: Solving the equation. For that the known and unknown components of \vec{F} and \vec{d} have to be separated. In this step the displacement boundary conditions are needed.

There are different possibilities to solve such a system. The most well known is Gauss elimination. But, analogously to the consideration made in the previous paragraphs, most of the processing time is ineffective handling of zeros.

It is possible to derive more informations from the solutions for the displacements and forces at the joints. This is called post-processing. All quantities described in chapter 3.2 (e.g. strains and stresses) can be calculated with the given equations. This is possible for the whole system, but also for single elements. To do that the system has to be disconnected again into its elements with their respective nodes.

Remark: This chapter only described plate bending, giving a basic idea of the DSM. To describe plate vibrations, the displacements and forces have to be dependent on the time and the position.

$$\vec{d} = \vec{d}(x, y, t), \quad \vec{F} = \vec{F}(x, y, t) \quad (62)$$

The displacements are described by a wave function, $\vec{d} \propto \exp[i\omega t]$, where ω is an eigenfrequency of the plate.

3.2.7 Computer implementation

An efficient computer implementation of Gauss elimination for sparse matrices is the frontal method[21]. Only a part of the matrix is analysed at a given time. This subset is called the front, hence the name of the method. In the front more efficient operations for dense matrices can be used.

It is possible to use the element stiffness matrices as fronts. Therefore the processes of connecting the elements, applying displacement boundary conditions and solving the global stiffness equation can be done in one step using this method.

An even more efficient way is the multifrontal method[22]. The basic ideas and steps are the same as in the frontal method. But different independent fronts, i.e. element stiffness matrices, can be processed at the same time. This allows for a better computer implementation, especially on multi-core systems.

In the following an estimation for the needed computer operations is given, to compare the classical approach and the frontal method. As an example the plate in figure 4 is taken. The mesh consists of 10000 elements. Each element has $n_e = 4$ nodes.⁶ For simplicity it is assumed that an element has only 4 degrees of freedom, which means that displacement and force at each node are 1-dimensional. The element stiffness matrices are 4×4 matrices, which results in $4 \cdot 4 \cdot 10000 = 1.6 \cdot 10^5$ matrix entries.

In the whole system 10000 nodes are in the center of the elements. Each element has 3 nodes in its corners, but each corner is shared by 6 elements (see figure 4, right). So there are approximately $10000 \cdot 3/6 = 5000$ nodes in the triangles' corners. There are some more nodes because of the boundary of the mesh, but this has not a big impact on the estimation. So the number of nodes in the system is $n_s \approx 15000$.

The classical approach: Extending all the element stiffness matrices to the size of the global stiffness matrix results in approximately $15000 \cdot 15000 \cdot 10000 = 2.25 \cdot 10^{12}$ matrix entries. At least $2.25 \cdot 10^{12} - 4 \cdot 1.6 \cdot 10^5$ of those values are 0.

To obtain the global stiffness matrix the extended element stiffness matrices have to be summed up (equation (61)). There are 10000

⁶Three nodes are enough to describe the geometry of the elements. But in the DSM at least four nodes are required for the interelement continuity of the solution. Usually three are placed in the corners and one in the center of the triangle.

element stiffness matrices with $2.25 \cdot 10^8$ entries each. This equals $2.25 \cdot 10^8 \cdot 10000 = 2.25 \cdot 10^{12}$ operations.

The global stiffness equation is solved with Gauss elimination. The number of operations for a $n \times n$ matrix is n^3 . The global stiffness matrix is a $n_s \times n_s$ matrix, so $n_s^3 \approx 15000^3 = 3.4 \cdot 10^{12}$ operations are needed.

The frontal method: The element stiffness matrices are diagonalized with Gauss elimination. Only $n_e^3 = 4^3 = 64$ operations per element stiffness matrix are needed, resulting in $6.4 \cdot 10^5$ operations for all of them.

The element stiffness matrices are merged into the global stiffness matrix by an array (called the element freedom table). This table can be seen as a map, which points each entry to its new position in the global stiffness matrix. The easiest way to obtain it is saving the position of each element and its nodes while disassembling the mesh into single elements. For that the position of each element and each node has to be assigned to a numerical value. Approximately 25000 values have to be saved.

The number of operations needed in the merging process is approximately $1.6 \cdot 10^5$. Note that the identifier described in the previous paragraph and the corresponding entry in the element freedom table has to be accessed for each entry, which increases the time needed for the operations.

Comparing these simple estimations for the two approaches yields: Processing time and especially needed storage space is lower in the frontal method by orders of magnitude 10^6 . Note that in the estimations of the numbers only arithmetic operations are counted. The application of boundary conditions is not considered, because it should not make a difference between the two methods.

4 Experimental setup

The schematic set up of the experiment is shown in figure 6.

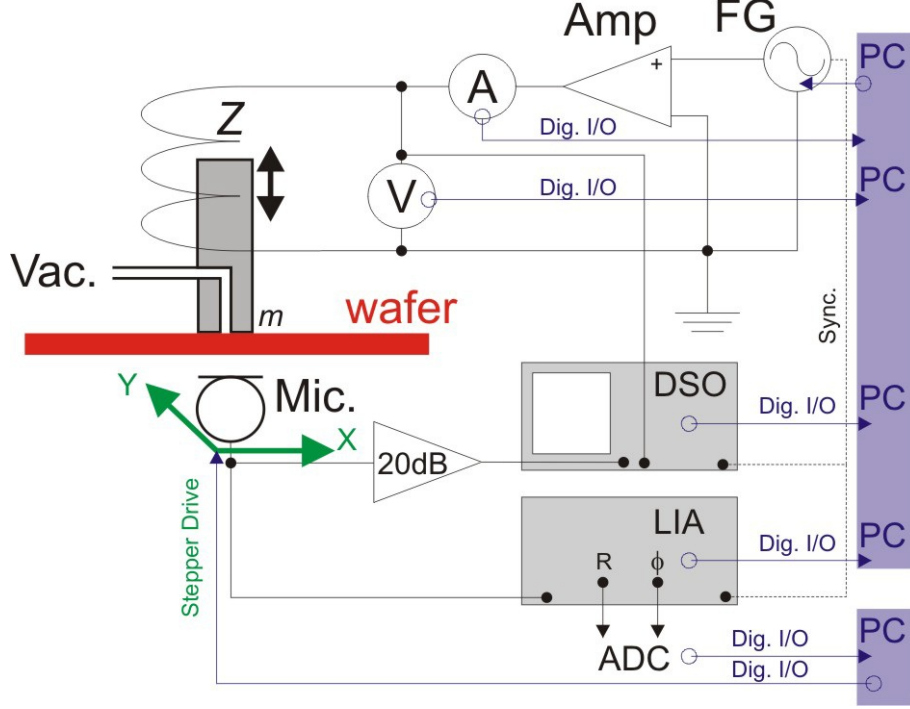


Figure 6: Circuit diagram of the experiment.

A PC is used to control a function generator (FG). An amplifier enhances the signal, which is used to induce vibrations via the coil of a loudspeaker. Current I and voltage U are measured by an ammeter and a voltmeter. The measurements are passed on to the PC.

The upper end of a plastic rod is attached to the loudspeaker. The lower end is hollow. The hollow room has two exits. One is connected to a vacuum pump. The other is located on the bottom area of the rod. A small plastic ring is attached there. The pump can vacuum a wafer against the ring, which reduces the area of connection between the wafer and the rod.

Below the wafer a microphone is attached to a motorized xy-stage. The position is controlled by the PC.

The signal of the microphone is analysed by a lock-in amplifier (LIA). The LIA's reference signal was obtained from the FG. Phase difference $\Delta\phi$ and amplitude of the microphone's signal are measured. With ϕ_g as the phase of the generated signal from the function generator and ϕ_m as the phase of the

signal from the microphone it is:

$$\Delta\phi = \phi_g - \phi_m \quad (63)$$

The data from the LIA are digitized by an analog-to-digital converter (ADC) and passed on to the PC.

A digital storage oscilloscope (DSO) is connected to the microphone and the amplifier. It is only used to obtain a first impression of the signals. The trigger signal for the DSO is taken directly from the function generator.

The setup of the experiment (without the electronics) is shown in figure 7.

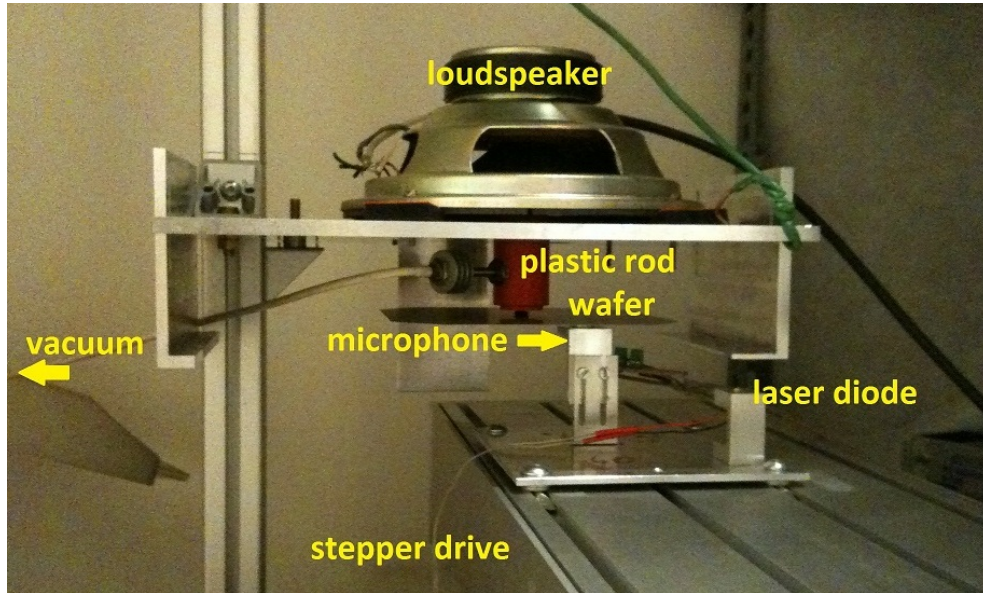


Figure 7: The experimental setup.

An aluminium plate is fixed to a pole. Fixated to this plate are:

- The loudspeaker. To prevent coupling of the vibrations from the loudspeaker in the plate, small pieces of foam material are used for isolation. The plastic rod can move freely through a hole in the plate.
- Three smaller plates: Two L-shaped plates on the sides and a flat one on the rear. Their purpose is to give a fixed position for another aluminium plate. This plate is used to change the wafer. On the plate three plastic bars mark the position for the wafer. The plate can be moved into the holder, placing the wafer's center exactly beneath the

center of the plastic rod. Then the wafer is lifted up and sucked to the plastic ring by the vacuum pump.

During the measurements with a wafer the vertical distance between microphone and wafer is fixed.

The laser diode is used as a reference point between the movable table (with the microphone on it) and the wafer. The position of the stepper drive is not fixed in relation to the position of the wafer. It is possible that the relative position is changed unintentionally. Thus, the previous setup can be restored again with the help of the laser diode.

A problem with this setup is the weight of the loudspeaker. Only one edge of the plate carrying the loudspeaker is clamped to the pole. It is pressed down at the free edges off a horizontal position. To counter this, a wire is attached to the edge on the opposite of the pole. By pulling at the wire the plate can be brought into a horizontal position. The upper end of the wire can then be attached to the pole.

4.1 Instruments

4.1.1 Accuracy

In the following the used instruments are described and their corresponding accuracies listed. Because the measurements range between 0.2 – 2.7 kHz, only the errors for that frequency range are noted.

FG: The FG is an Agilent 33200A Function / Arbitrary Waveform Generator. It can create a sinusoidal AC signal from 1 μ Hz to 20 MHz. Its total harmonic distortion for sine waves up to 20 kHz is 0.04 %. The *Sync* output on the front is connected to the LIA and the DSO, the *Output* output to the amplifier. After [23].

Amplifier: The amplifier is a Bremi BRS-26. Because it is a homemade device, there is no data sheet available. It is only suited for positive voltages between (0 – 10) V. Thus the offset of the FG is set to +1 V during the measurements.

Ammeter: The ammeter is an Agilent 34401A 6 1/2 Digit Multimeter. Its accuracy is:

$$\begin{aligned}
 &\pm (0.1\% + 0.04\%) \\
 &\pm (0.015\% + 0.006\%) \quad \text{temperature coefficient per } ^\circ\text{C} \\
 &\pm (0.18\% + 0) \quad \text{additional low frequency error, up to 1 kHz} \\
 &\pm (0 + 0.002\%) \quad \text{sinewave transfer accuracy}
 \end{aligned}$$

The first value denotes the error in % of the reading, the second value the error in % of the range. The temperature coefficient only has to be accounted for temperatures higher than 28 °C or lower than 18 °C. Thus it is discarded. After [24].

Voltmeter: The voltmeter is a Fluke 45 Dual Display Multimeter. Its accuracy is:

$$\pm(0.5 \% \text{ of the reading} + 2 \text{ digits})$$

These values are given for a temperature between 18 – 28 °C. After [25].

LIA: The LIA is a Stanford Research Systems Model SR530.

The microphone is plugged into the signal input *A*. The signal channel has a full scale sensitivity between 100 nV – 500 mV in 24 ranges. The noise is $7 \text{ nV}/\sqrt{\text{Hz}}$ at 1 kHz. The gain accuracy between 2 Hz and 100 kHz is 1 %.

The reference signal input is connected to the FG. The reference channel is able to process signals with frequencies between 0.5 Hz – 100 kHz. The acquisition time is between 6 s at 10 Hz and 2 s at 10 kHz. The phase error is less than 1° above 10 Hz. An additional phase drift originating from temperature differences is discarded in the data evaluation.

The DC output signal has a full scale of $\pm 10 \text{ V}$. The signal from channel 1 is proportional to the amplitude of the signal from the microphone. The signal from channel 2 is proportional to the phase difference $\Delta\phi$. The offset is set to 0 for both outputs. After [26].

DSO: The DSO is a Tektronix TDS 2022B. The amplifier's signal is plugged in to channel 1, the microphone's signal in to channel 2. The trigger input is connected to the FG's *Sync* output. Its purpose is only to monitor the signals. Thus the accuracy is not important for the data evaluation.

Microphone: The microphone is a LEM EM100T. It is a non-directional electret condenser microphone. Its supply voltage during the measurements is 6 V. The sensitivity, given for 1 kHz, is $6.3 \text{ V} \pm 3 \text{ dB} / \text{Pa}$. After [27].

4.1.2 Loudspeaker

The loudspeaker is a Hornsonic 16L25. The important characteristic is the displacement w_m of its membrane in relation to the power $P = U \cdot I$.

To measure the displacement of the membrane (and thus of the plastic rod attached to it) a Heidenhain length gauge is used. It is fixed to the table beneath the plastic rod. Small movements of the rod push the gauge head further down.

The FG creates a DC signal. Current and voltage at the speaker are measured. The measurements are shown in table 1. U_{DC} is the voltage of the signal from the FG, U the measured voltage, I the measured current and w_m the displacement of the rod.

$U_{DC}[\text{mV}]$	700	800	900	950	1000	1050	1100	1150	1200
$U[\text{mV}]$	144	239	337	387	437	487	538	589	630
$I[\text{mA}]$	22.5	37.4	52.7	60.5	68.3	76.2	84.1	92.1	100
$w_m[\mu\text{m}]$	4	4	10	15	20	27	34	40	49
$U_{DC}[\text{mV}]$	1250	1300	1320	1300	1200	1100	1000	900	800
$U[\text{mV}]$	691	742	1300	1270	1099	928	758	358	259
$I[\text{mA}]$	108	116	201	197	170	144	118	55.7	40
$w_m[\mu\text{m}]$	58	66	179	185	185	185	170	108	88

Table 1: Measurements of the speaker’s displacement for different voltages.

The results are tabulated in chronological order. A big jump in the measured voltage U , current I and the displacement w_m is seen, when the voltage U_{DC} is changed from 1300 to 1320. Reducing U_{DC} after the jump results in different U and w_m than before. This effect does not diminish until 900 mV. The speaker seems to not respond well to DC signals. Thus it is hard to measure the displacement of the membrane for different voltages. However limits of the displacement can be estimated.

4.2 Samples

The samples are pseudo-square monocrystalline silicon wafers from *Falcon-cell*. Their properties are shown in table 2.

Crystallographic orientation	(100)
Circular diameter	$(150 \pm 1) \text{ mm}$
Square size	$(125 \times 125 \pm 0.5) \text{ mm}$
Thickness	$(230 \pm 20) \mu\text{m}$

Table 2: Properties of the used wafers according to the manufacturer.

The thickness varies strongest of the geometrical properties between the wafers. Thus it is measured for each wafer with a Heidenhain length gauge.

For that the gauge is fixed over a glass plate, so that the gauge head touches it. This value is set to 0. Then the wafer is brought between plate and gauge head. The wafers are measured on 9 different positions. With this method possible nonuniformities in thickness can be seen, and it is possible to gain a more exact average value.

Another possibility is to calculate the thickness h_w of the wafers using their volume, mass m_w and density ρ_{Si} . Assuming a uniform thickness across the wafer it is:

$$\rho_{Si} = \frac{m_w}{h_w A_w} \Rightarrow h_w = \frac{m_w}{\rho_{Si} A_w} \quad (64)$$

To determine its ground area A_w , a wafer is scanned. Every pixel of the background is colored white, every pixel of the wafer is colored black. The picture is cut to the size which corresponds to the wafer's square 125×125 mm. So the ratio between number of pixels in the whole picture and number of white pixels is the same as the ratio between the area of a 125×125 mm square and the missing corners.

From 2190400 pixels in the picture 117898 are white. Thus the ground area A_w is:

$$A_w = (125 \text{ mm})^2 \cdot \left(1 - \frac{117898}{2190400}\right) \approx (125 \text{ mm})^2 \cdot 0.946 \approx 14784 \text{ mm}^2 \quad (65)$$

The mass is measured using a Sartorius weighing scale. The measurements are shown in table 3. The density of silicon is 2328 kg/m^3 [28].

Wafer	m_w [mg]	h_w [μm] calculated	h_w [μm] measured	variation of h_w [μm]
1	7880.8	238.1	243.7	10
2	7785.7	235.2	238.1	6
3	7829.9	236.5	237.7	9
4	7651.4	231.2	238.6	8
5	7693.9	232.4	239.2	7
6	7891.1	238.4	243.2	11
7	7773.7	234.8	239.9	7
8	7814.1	236.1	241.0	7
9	7806.1	235.8	238.8	8
11	7725.6	233.4	237.9	9
12	7825.0	236.4	241.5	6

Table 3: Measurements of the wafers's mass and thickness. The variation of h_w [μm] is the difference between smallest and biggest measured value.

Note that for every wafer the calculated thickness h_w is smaller than the measured one. This is due to the roughness of the wafers' and the glasses' surface. Thus the measurements differ from h_w .

The mass of the wafer can be measured more accurately than its thickness. The length gauge has a resolution of $\pm 1 \mu\text{m} \hat{=} \sim 0.4\%$ of the measurement. The weighing scale has a resolution of $\pm 0.1 \text{ mg} \hat{=} \sim 0.001\%$ of the measurement. In addition to the fact that they are not shifted, the lower values of h_w are more accurate and have a smaller error.

4.3 Measurements

The samples are measured:

- with a fixed microphone position and variable frequency;
- with a fixed frequency and variable microphone position;
- again in both setups after surface cracks are added to the wafer.

Afterwards the measurements for the wafers with and without cracks are compared. The amplitude of the FG's output is kept constant during the measurements on a single wafer.

Two samples are measured 3 times each without adding cracks to the wafers. Then the results of the measurements are compared. Using this method an estimation of the impact of the wafer loading and unloading procedure can be given, e.g. due to a small variation in the position.

4.3.1 Variable frequency

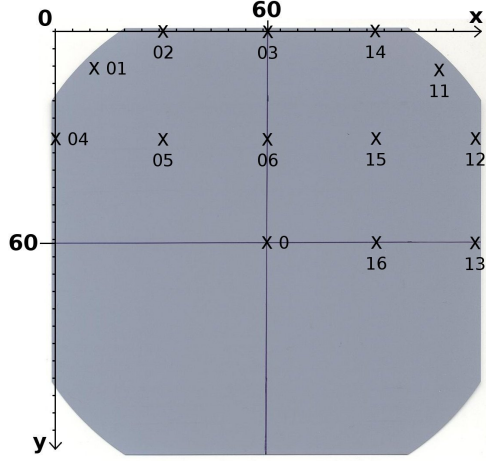
For the first set of measurements the microphone's position is fixed. The oscillations are induced with variable frequencies between 200 Hz and 2.7 kHz. Every 5 Hz amplitude U_m and phase ϕ_m of the microphone's signal, voltage U and current I are measured. This way the resonant frequencies of the wafer are found.

For a higher accuracy, the vicinity of the amplitude peaks (usually a range of $\sim 50 \text{ Hz}$) is measured in steps of 1 Hz. For an even better resolution, the top of the amplitude peak (usually a range of $\sim 2 \text{ Hz}$) is then measured in steps of 0.1 Hz.

Because the LIA needs time to adjust to new frequencies (see chapter 4.1.1), these measurements take some time. Thus only the proximity of the amplitude peaks is measured in a higher resolution and not the whole frequency spectrum.

These measurements are repeated for several positions of the microphone below the wafer. Table 4 shows these positions.

All the following information is given in the coordinate system shown in figure 8.



Reading point	Position [mm]
0	(60, 60)
01	(10, 10)
02	(30, 0)
03	(60, 0)
04	(0, 30)
05	(30, 30)
06	(60, 30)
11	(110, 10)
12	(120, 30)
13	(120, 60)
14	(90, 0)
15	(90, 30)
16	(90, 60)

Figure 8: One of the wafers used in the measurements. All position informations in the following are given in the Cartesian coordinate system shown. The point $(x, y) = (60 \text{ mm}, 60 \text{ mm})$ marks the center of the wafer.

Table 4: Measurement points (MPs).

4.3.2 Variable position

After the resonant frequencies of a wafer are determined, oscillations are induced with one of these frequencies. The position of the microphone is constantly changing while the plate is scanned. 600×600 measurements (equal to an area of $120 \times 120 \text{ mm}$) are taken for the wafers 1-5. 620×620 measurements (equal to an area of $124 \times 124 \text{ mm}$) are taken for the wafers 6-12.

Note that during the data evaluation 13 measurements per row have to be deleted. The reason is: The microphone starts in the top left corner, position $(x, y) = (0, 0)$, and moves to the top right corner at $(124, 0)$. Then it is positioned in the next row to $(124, 0.2)$ and moves to $(0, 0.2)$ in opposite direction, and so on. So the whole plate is scanned row by row. Because the electronics processing the signal need some time, the measured signals between two subsequent rows are displaced by 13 points. This can be corrected

afterwards, but some measurements are lost in the process.

4.3.3 Wafer displacements

The measurements described in the previous chapter yield a 607×620 grid of values. The values are proportional to voltage U_m and phase ϕ_m of the microphone signal, not to the displacements $w(x, y, t)$ of the wafer. In this chapter the basic assumptions and calculations needed to obtain the displacements from the signal are outlined.

The oscillations in the plate are induced with the frequency ω . Thus it is assumed that the whole plate vibrates with ω . Each point of the plate's surface can be seen as a point source for a sound wave, which propagates through the air. All the sound waves with the same frequency superpose. Interference effects can be seen.

The microphone measures the sound pressure p_s . It is inversely proportional to the distance of the sound source r_m .

$$p_s \propto \frac{1}{r_m} \quad (66)$$

So the sound pressure caused by the oscillation of the plate directly above the microphone has the biggest impact on the measurement. But each measurement gives information about the oscillations of the whole plate.

To calculate the wafer's deflection, the square circumscribing the wafer is divided in 0.2×0.2 mm big squares.⁷ Each single point of the measurement $(U_m)_{ij}$ is connected to the displacements w_{kl} of the whole plate with a coefficient matrix \mathbf{G} . The indices $i, k = 1, 2, \dots, 607$ describe the x -position. The indices $j, l = 1, 2, \dots, 620$ denote the y -position.

$$(U_m)_{ij} = \sum_{kl} G_{ijkl} w_{kl} \quad (67)$$

The coefficients can be obtained by looking at the geometry of the setup and wave propagation. Then equation (67) has to be solved. It is a linear equation system with $607 \cdot 620$ unknowns.

Two additional informations are given:

- The deflection in the wafer's missing edges is 0.
- The deflection in the middle of the wafer, where it touches the ring, is known. It is equal to the deflection of the speaker's membrane.

⁷This value is chosen because each 0.2 mm a measurement is taken, see chapter 4.3.2.

But additional effects, e.g. turbulences in the air at the wafer's edges and interference of the sound waves, make it almost impossible to obtain exact results for the displacements. Therefore, and because of the difficulties measuring the displacement of the speaker dependent on the power of the FG's signal, these calculations are discarded.

In the evaluation of the oscillation patterns a simple approximation for the displacements of the plate w_{ij} is made: For the same frequency they are proportional to the measured signal $(U_m)_{ij}$.

$$w_{ij} \propto (U_m)_{ij} \quad (68)$$

4.4 Laser cutting

In order to add surface cracks to the wafer a laser scribing machine is used. It is a Yuemao Laser YMS-50 porcelain lamp pumped laser scribing system. The frequency is set to 8.8 kHz, the beam power to 6.8 W. The scribing speed is varied between 18 mm/s and 24 mm/s.

To measure the cutting depth, two wafers are cut with each of the cutting speeds listed above. Then they are broken along the cuts. With a microscope the fracture area is magnified (shown in figure 9). The thickness of the wafer can be measured. The depth of the cut can be obtained from the thickness and the ratio between the depth of the cut and the depth of the breakage. It is $(100 \pm 15) \mu\text{m}$ for the higher cutting speed and $(125 \pm 15) \mu\text{m}$ for the lower cutting speed. The error is estimated from the pictures. The form of the cuts is shown in the figures 10-16.

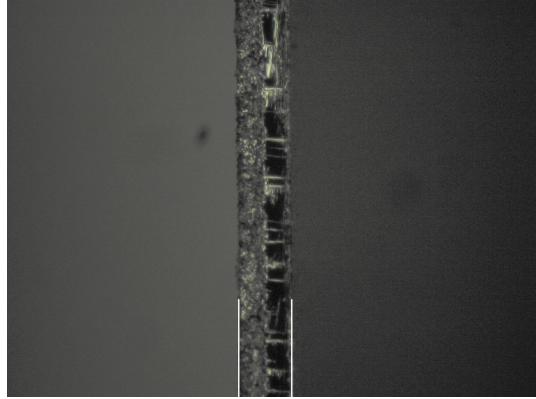


Figure 9: The fracture area magnified. The thickness of the wafer shown in the figure, which is the distance between the two white lines marking its edges, is $\approx 235 \mu\text{m}$. On the left side is the lasercut, on the right side the breakage area.

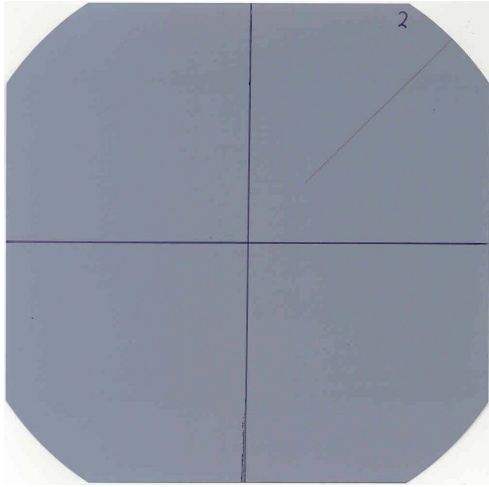


Figure 10: Wafer 2, processed with a cutting speed of 18 mm/s . The cut on wafer 1 has the same form and size, but was made with a cutting speed of 24 mm/s .

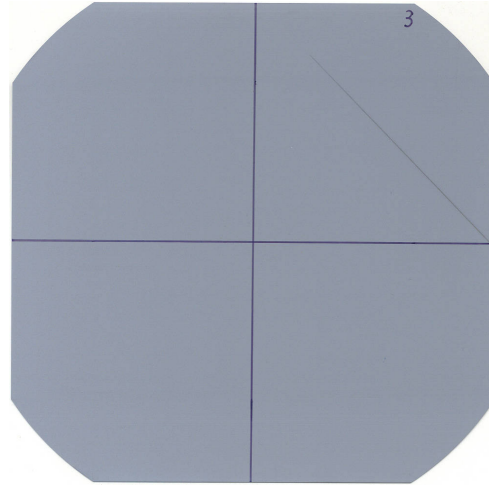


Figure 11: Wafer 3, processed with a cutting speed of 18 mm/s . The cut on wafer 4 has the same form and size, but was made with a cutting speed of 24 mm/s .

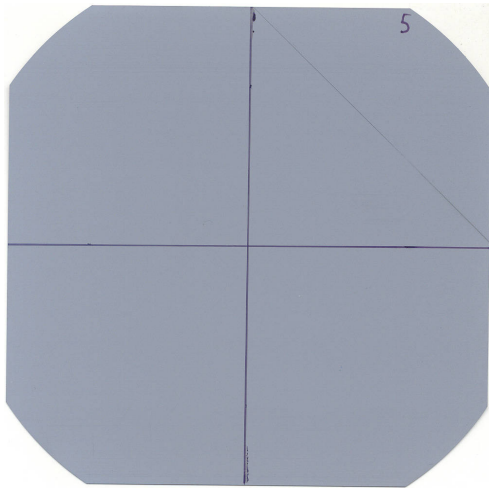


Figure 12: Wafer 5, processed with a cutting speed of 24 mm/s .

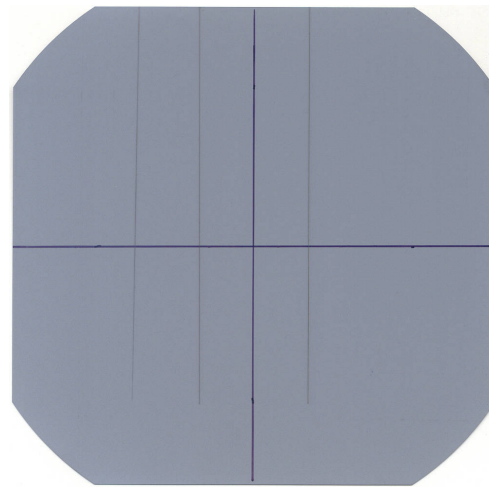


Figure 13: Wafer 6, processed with a cutting speed of 18 mm/s . The number denoting the wafer is on the back side, on the top left corner, as it is on the wafers 7, 8 and 9.

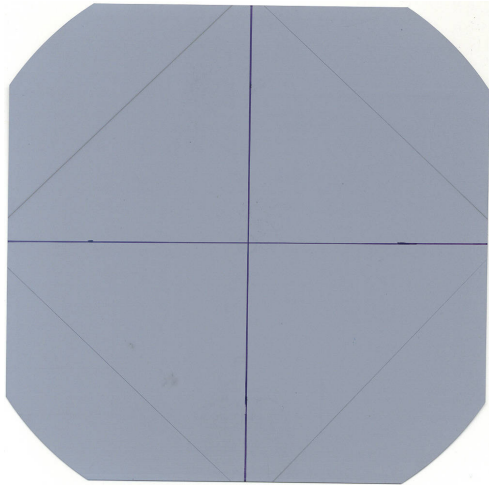


Figure 14: Wafer 7, processed with a cutting speed of 18 mm/s .

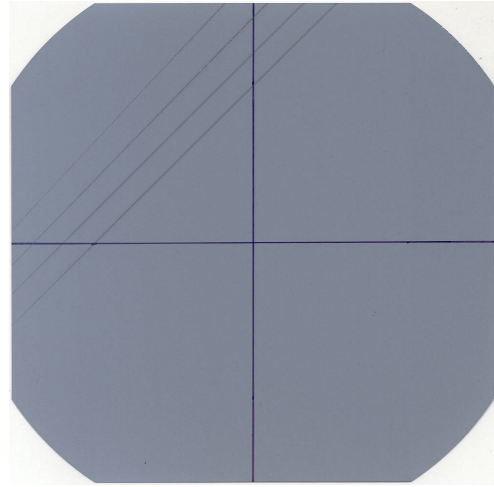


Figure 15: Wafer 8, processed with a cutting speed of 18 mm/s .

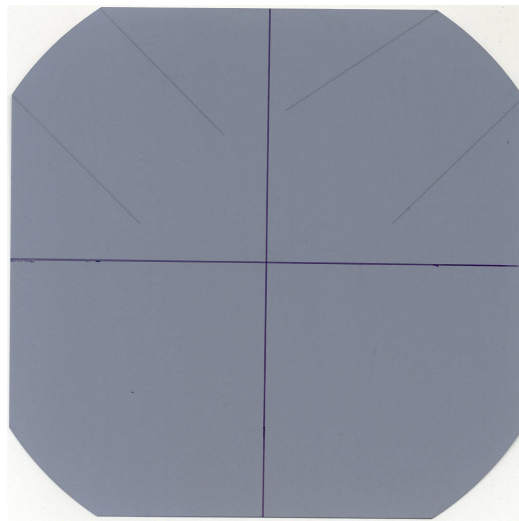


Figure 16: Wafer 9, processed with a cutting speed of 18 mm/s .

4.5 Simulation

The purposes of the FEA for this thesis are:

- to compare the simulations to the experimental results;
- to test the applicability of the Kirchhoff plate bending theory to the wafers. This has to be analysed, because the wafers do not comply with all of Kirchhoff's hypotheses.

One of the big problems of FEA is: "The method is poorly adapted to a solution of the so-called singular problems, e.g. plates and shells with cracks"[15]. Thus, the simulations are done only for the uncracked wafers and the results are compared to the experiment.

The FEA program used is the *Elmer* software[16].

The wafer is modelled with *ElmerGrid*. The mesh is shown in figure 4. The file can be found in Appendix A.3.

The physical properties and simulation parameters are added with *ElmerGUI*. They are shown in table 5.

Then the equations are solved with *ElmerSolver*. The results can be viewed in the postprocessor VTK - the internal visualization toolkit in ElmerGUI - or in ElmerPost, the post-processor of the Elmer software.

Menu point	Option	Set to
Setup	Simulation type	steady state
	Steady state max iterations	1
Equation - elastic plates	Active	on
Solver specific options	Eigen analysis	on
	Eigen system values	50
Linear system	Direct	on, Umfpack ⁸
Material	Density	2328
	Young's modulus	$1.3 \cdot 10^{11}$
	Poisson ratio	0.28
	Thickness	varied
	Tension	0
Boundary Condition	Deflection 1	0
(Boundary 1)	Deflection 2	0
	Deflection 3	0

Table 5: The options used for the FEA in ElmerGUI.

Some additions have to be made:

- All values are given in SI units: The density is given in $[\text{kg}/\text{m}^3]$ and Young's modulus in $[\text{N}/\text{m}^2]$.
- The thickness is varied to match the thickness of the different wafers. It is constant for a single wafer.
- The plate vibration simulations in Elmer can only be done for isotropic materials. Thus only one value for Young's modulus can be added. This difference to the experiment, where anisotropic c-Si is used, has to be considered when comparing experimental results and simulation.
- The values for Young's modulus and Poisson ratio are taken from [30] for the orientation (100).
- The deflection of the boundary in the middle of the mesh (equivalent to the part of the wafer coupled to the excitation source) is set to 0. Thus, the oscillation patterns in the simulations are in the CS of the vibrating speaker membrane.

In the experimental setup the microphone is fixed to a table and does not vibrate. Therefore the measurements are in the laboratory frame of reference. This difference has no impact on the resonant frequencies. Because of the problems to calculate the deflection of the plate described in the chapters 4.1.2 and 4.3.3, the difference of the deflection between simulation and experiment are of no further interest.

- ElmerSolver shows the resonance frequencies squared ω^2 as a result. This has to be considered when comparing the results between experiment and simulation.

A more detailed description of the programs and the steps necessary can be found elsewhere[16].

⁸"UMFPACK is a set of routines for solving unsymmetric sparse linear systems [...] using the Unsymmetric MultiFrontal method." [29]

5 Data evaluation

In this chapter, at first an overview over the measured frequency spectrum and oscillations is given. Later the measurements of the wafers and those of the cracked wafers are compared.

5.1 Introduction

5.1.1 The frequency spectrum

The first set of measurements, investigating oscillations at frequencies between 200 Hz and 2.7 kHz, is taken at MP 0. These measurements, with the resolution of 5 Hz, give an approximate frequency range of the peaks. The same frequency spectrum was analysed at other MPs, but no additional resonance frequencies were observed.

The displacement of the wafer at MP 0 is the same for all frequencies. This MP is directly below the plastic ring connecting wafer and piston. But, because of the considerations in chapter 4.3.3, the voltage peaks of the microphone's signal are still visible.

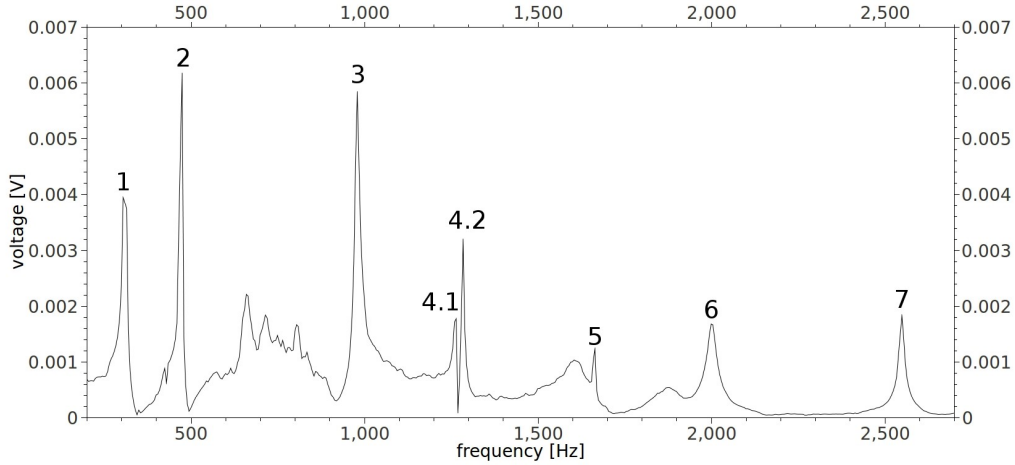


Figure 17: The enumeration of the peaks.

Each major peak enumerated in figure 17 is the result of a resonant oscillation. There are other, weaker peaks, for example between 600 – 900 Hz. They do not only differ by magnitude, but also by bandwidth. The measurements for this thesis are focused on the major peaks.

Remark: The number of the wafers, which are depicted in the figures, are given in the table of figures in appendix A.5.

5.1.2 Basic considerations

Before looking at the corresponding oscillation patterns, some remarks and considerations have to be made.

Color scale: The frame of reference differs between measurement and simulation (see chapter 4.5). Thus, it was foregone to convert the results to a single scale.

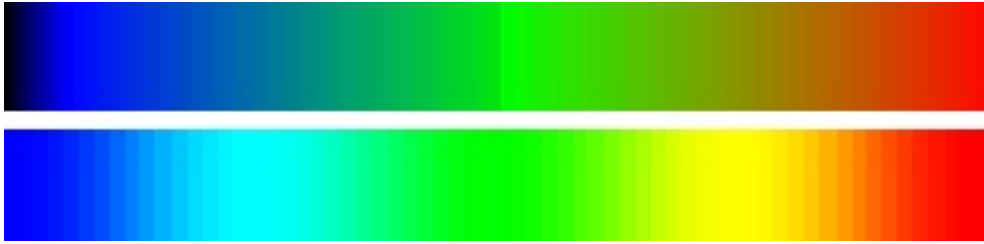


Figure 18: Top: The colors, in a linear scale, used in the following for displaying the measured oscillation patterns. Where relevant, the smallest value (black) and the highest value (red) are given in tables or in the descriptions of the corresponding pictures.

Bottom: The colors, in a linear scale, from the ElmerPost VTK. They are used to show the simulated oscillation patterns.

The signed amplitude: The data from the measurements contains information on the amplitude of the microphone's signal U_m and on the phase difference between the microphone's and the FG's signals $\Delta\phi$. To obtain the oscillation pattern, U_m has to be multiplied with the sign of $\Delta\phi$. In the following this is referred to as the signed amplitude U_s . It is, for a fixed frequency, seen as proportional to the deflection w of the plate.

$$w \propto U_s = U_m \cdot \text{sgn}(\Delta\phi) \quad (69)$$

But $\Delta\phi$ is shifted due to the electronics involved in the data processing. The LIA's output between -10 V and 10 V is proportional to the phase difference. If $\Delta\phi$ reaches one of those boundaries, equal to $\pm\pi$ [rad], it jumps to the other boundary⁹. This signal is then digitalized and saved. After that the jump is still visible in the saved data. Thus the phase difference has to be corrected accordingly.

⁹Theoretically, the jump only occurs when one of the boundaries $\pm 10\text{ V} \propto \pm\pi$ is reached. But due to an inaccuracy of the LIA it occurs at smaller values. This has to be considered in the correction of the phase difference.

A possible solution is to add the width of the spectrum, 2π , to all points below a threshold. Then from all values half the width of the spectrum is subtracted. Depending on the settings of the LIA, some peaks need to be corrected, whereas others do not.

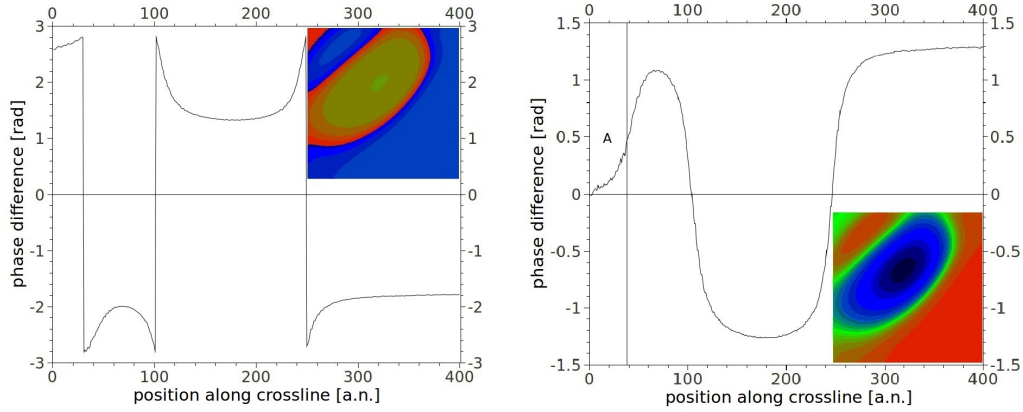


Figure 19: As an example, the phase difference of peak 3 is corrected. Only the upper left quarter of the wafer is depicted. The two small pictures show $\Delta\phi$ in that area. The graphs show the values for $\Delta\phi$ along a diagonal crossline from the top left to the bottom right corner.

The left side presents $\Delta\phi$ as obtained from the measurements. The jumps between the boundaries are visible, for example approximately at position 100.

The right side shows the same curve after the correction. The fast, but constant changes in $\Delta\phi$ near nodal lines are visible, for example near position 100. The area denoted with A in the graph is outside the edge of the pseudo-square wafer. $\Delta\phi$ approximates 0.

A problem with this method arises when applying it to the oscillations at higher frequencies. The reason for this is a measurement error, which sometimes occurs at nodal lines. Near nodal lines $\Delta\phi$ changes very fast. Especially the more complex oscillation patterns lead to a high derivation of $\Delta\phi$ in a small zone. The electronics, which record and evaluate the signal, cause some erroneous measurements in this zone. Instead of a strong, but constant change of $\Delta\phi$, or a jump between the boundaries, the value is set to 0. This is shown in figure 20.

Thus, only the amplitude U_m is taken in the comparison of the oscillation patterns in chapter 5.3.

The Chladni patterns: The sand in the experiments of E.F.F. Chladni[11] accumulated in the nodal lines. Therefore, the resulting patterns of the nodal lines on the oscillating plate are named after him. The phase difference is more or less constant, but it changes rapidly near the nodal lines (see figure 19, right side). Thus, $\Delta\phi$ can be derivated to obtain the corresponding Chladni pattern.

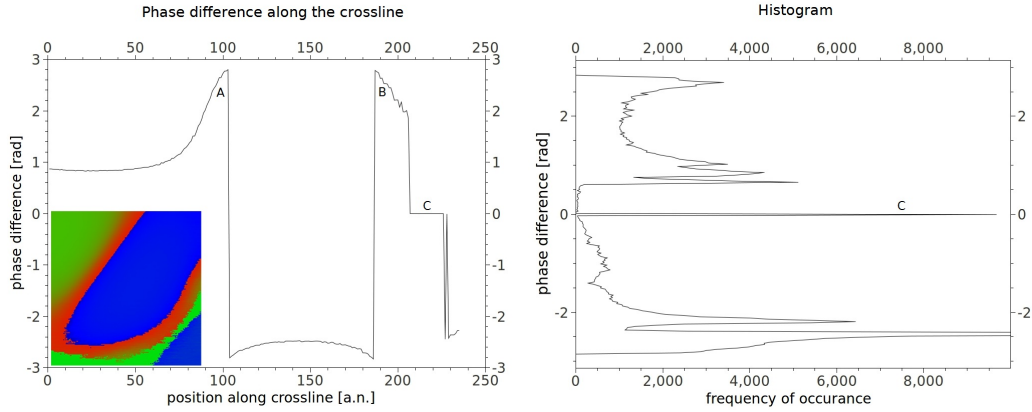


Figure 20: On the left side the bottom right corner of the wafer at peak 6 is shown. The graph shows $\Delta\phi$ along a diagonal crossline from the top left to the bottom right of the picture. Two of the jumps, denoted with A and B, are measured correctly. The third one, C, is not. Thus, $\Delta\phi$ in the vicinity of that nodal line is set to 0.

On the right side a histogram of $\Delta\phi$ of the whole wafer is shown. The erroneous measurements result in the strong peak C at $\Delta\phi = 0$. Near the upper and lower limits of $\Delta\phi$ ($\pm\pi$), no points are measured. This is due to the inaccuracy of the LIA close to the limits, resulting in earlier jumps.

5.1.3 Oscillation patterns and Chladni figures

In this chapter, the measured and simulated oscillations are shown, along with the corresponding Chladni patterns. In the pictures of the Chladni patterns a grey scale is used, with black as minimal and white as maximal values.

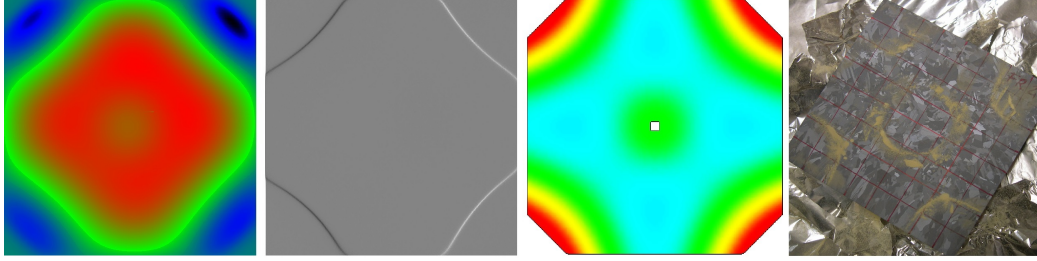


Figure 21: The first picture shows the measured oscillation pattern of the first resonance peak. The second picture shows the corresponding Chladni figure. The third picture shows the simulated oscillation pattern. The fourth picture shows the Chladni figure, visualized with clubmoss spores on a square multicrystalline silicon wafer (experiment by Mag. G.Zechner).

The dark and bright lines in the picture of the Chladni patterns are both showing the position of the nodal lines. The difference is a result of the derivation of $\Delta\phi$. The derivation can have a maximum or minimum along these lines, depending on the course of $\Delta\phi$.

The discrepancies of $\Delta\phi$ between measurement and simulation are caused by the boundary condition used in the simulation. There, the displacement of the wafer along the connection between wafer and plastic ring is set to 0. In the experiment the center of the wafer oscillates in the same phase as the loudspeaker. The sign of $\Delta\phi$ does not change until a nodal line is reached. This discrepancy leads to the possibility of a phase inversion between simulation and experiment.

Another difference can be observed near the edges of the wafer. There are the highest deflections in the simulation. In the experiment the central area of the wafer oscillates stronger than its edges. There are two reasons for this discrepancy. One is the boundary condition, which leads to a change of the frame of reference between experiment and simulation (see chapter 4.5). The other is caused by the nature of the measurements with the microphone (see chapter 4.3.3).

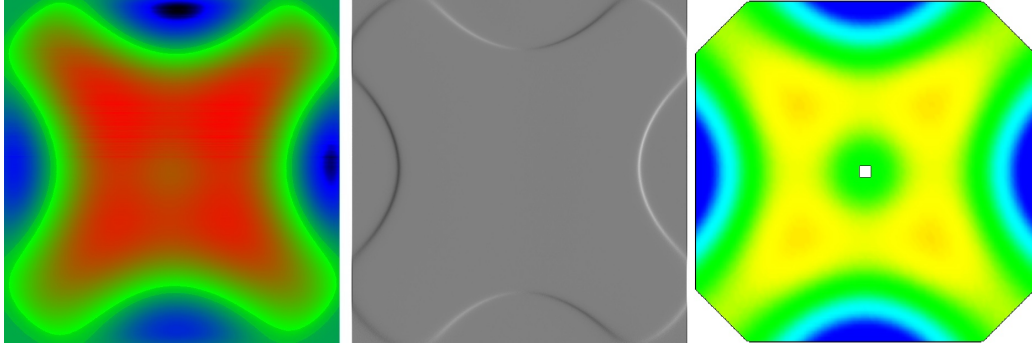


Figure 22: Wafer oscillation at peak 2.

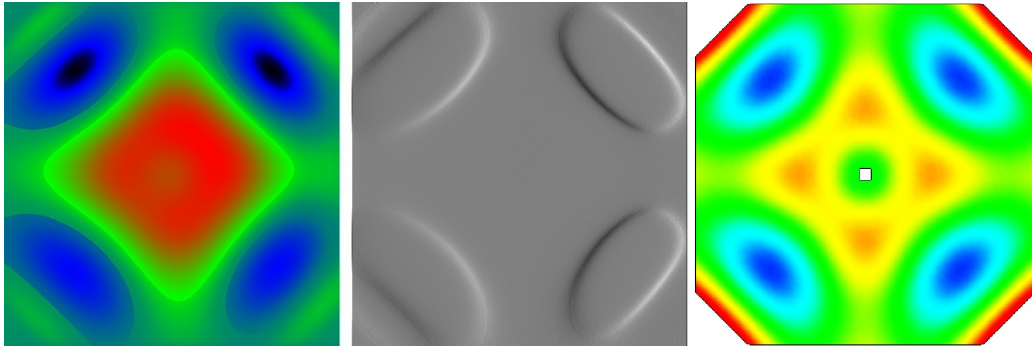


Figure 23: Wafer oscillation at peak 3.

In the measured oscillation patterns on the left in the figures 21-27, a small jump of U_s is visible along the nodal lines. Theoretically, the amplitude of the microphone's signal is 0 at a nodal line. But actually the signal is a little above 0, due to the nature of the measurements with the microphone. This causes a jump of U_s where the sign of $\Delta\phi$ changes, which is along the nodal lines.

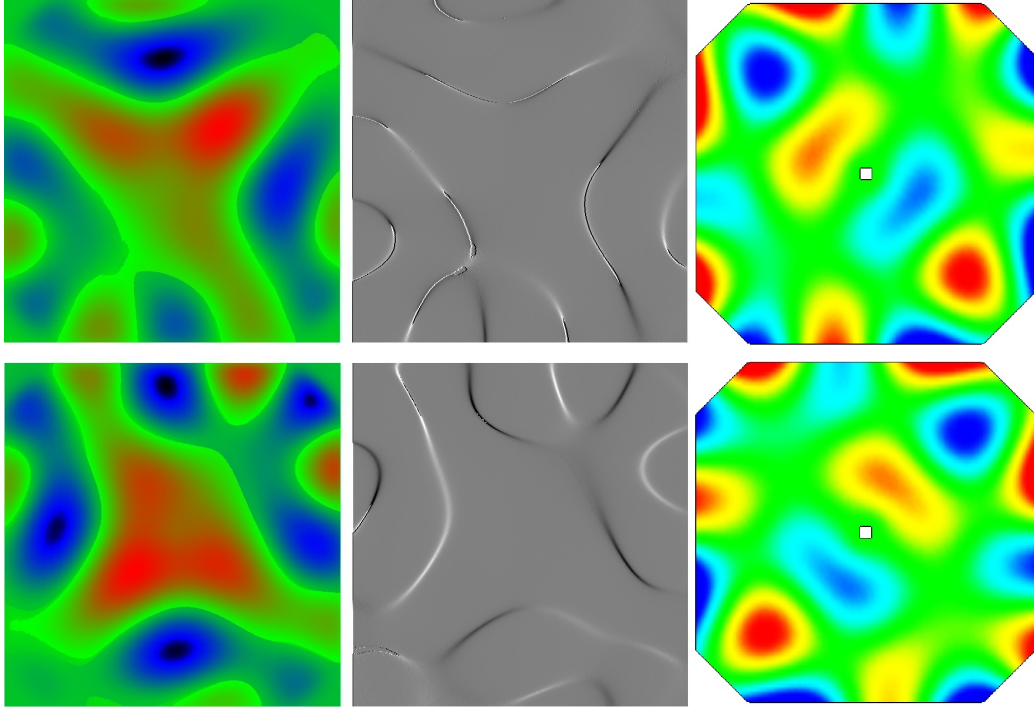


Figure 24: The first two pictures show the measured wafer oscillations and Chladni patterns at peak 4.1 (top) and at peak 4.2 (bottom). The pictures of the simulation show two oscillations in that frequency region. The gap between the resonance frequency of these oscillations is ≈ 0.5 Hz. The gap between the two peaks in the measurements is ≈ 20 Hz.

In the oscillation patterns, strong differences between the simulation and the measurements can be seen. The possible reasons for this are:

- In the simulations, a nodal line runs through the center of the wafer. In the experiment, at this position the oscillations are induced. Thus a nodal line, id est a minimum of the displacement of the wafer, at this point is not possible.
- The frequency gap between the two simulated peaks is very small. They can not be measured separately. Thus, both oscillations influence both measurements.

The white and black lines in the Chladni patterns are caused by measurement errors of $\Delta\phi$, which result in a maximum (white) or minimum (black) of the derivation.

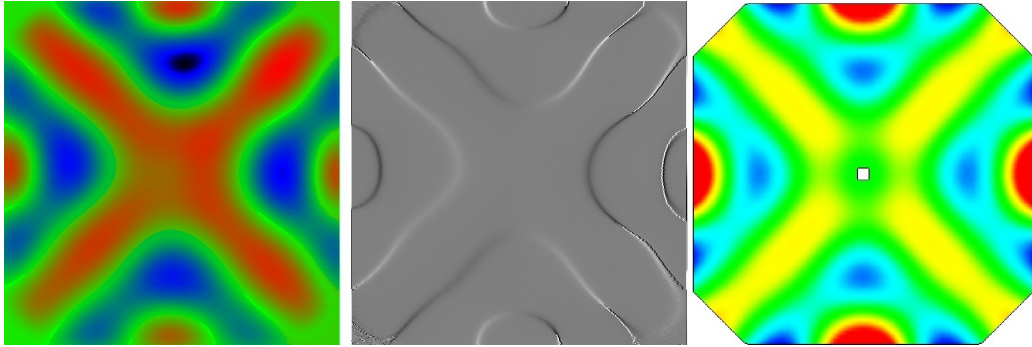


Figure 25: Wafer oscillation at peak 5.

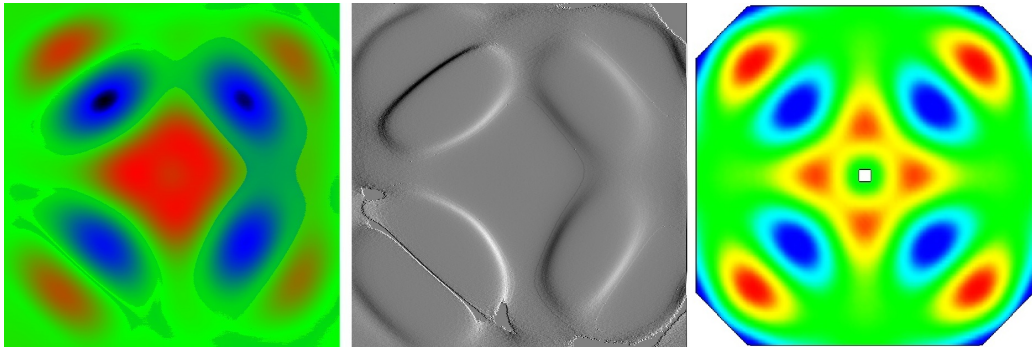


Figure 26: Wafer oscillation at peak 6.

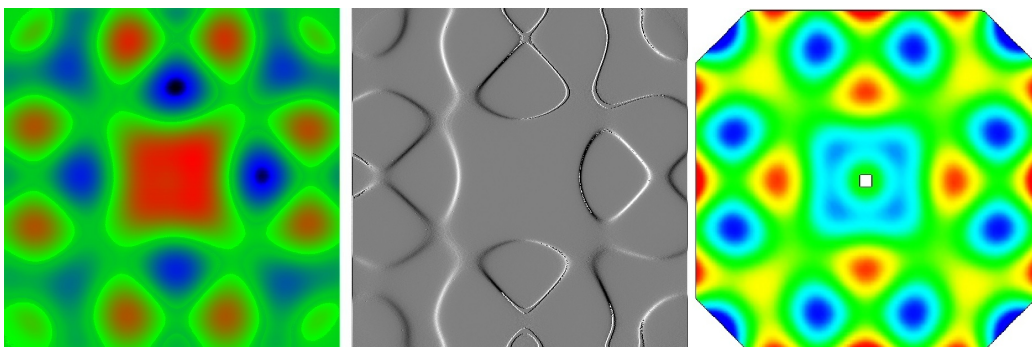


Figure 27: Wafer oscillation at peak 7.

5.2 Variable frequency

5.2.1 Microphone signal - voltage

The second set of measurements with a variable frequency includes a range of ≈ 50 Hz near the resonance frequencies with a resolution of 1 Hz.

There are differences in the measured microphone voltage between wafer and cracked wafer. Depending on the position of the wafer, the strength and form of the differences vary. The main observations are:

Amplitude: The maximum of the measured voltage does not vary consistently for most wafers. Only wafer 7 shows a constant change for all MPs and oscillations.

The measurements provide information about 13 fixed MPs of the oscillation patterns. Therefore, a conclusion for the whole pattern based on these points is impossible. Thus, the analysis of the amplitude is made with the data of the measurements with variable microphone position.

Half width: Cracks in thin plates can cause an increase of the full width at half maximum of resonance peaks. The main reason is a microslipping at the crack face walls, leading to a damping of the system. To a smaller extent also a reduction in the stiffness causes damping. Microslipping is minimized for surface notches, depending on the length of the notch [4 and references therein]. In [4] the effect was observed at the second resonance peak.

This could not be reproduced in the measurements for this master thesis. The full width at half maximum is the same for the wafers with and without cracks.

The reasons for this discrepancy are:

- Only surface notches are added as cracks. Thus, effects which cause damping of the oscillations are minimized.
- The two experiments differ in the boundary conditions and the excitation source. In my measurements the edges of the wafer are free. A loudspeaker is used to induce oscillations. In [4] one edge of the plate is free, three are clamped. A non-contacting electromagnetic driver is used to stimulate vibrations. This leads to different oscillation patterns, which are influenced differently by specific cracks.

Mode splitting: Residual stress, as a result of the wafer manufacturing process, has impacts on the measurements. Mode splitting occurs for non-

uniform residual stress distributions. The resonance frequencies of the wafers increase with increasing stress[3].

In my measurements mode splitting can not be observed. Thus, it is concluded that the wafers have uniform stress distributions.

Resonance frequency: The resonance frequency does not change for all oscillation modes, except for 4.1 and 4.2.

Peak 4: Very strong differences can be observed at the double peak 4, shown in figure 28. This is the only peak where a resonance frequency shift can be observed constantly. The reason for this is the overlapping of two different peaks in this frequency range. The sum of both resonance frequencies of the peaks 4.1 and 4.2 behaves like the resonance frequency of other peaks and is almost constant.

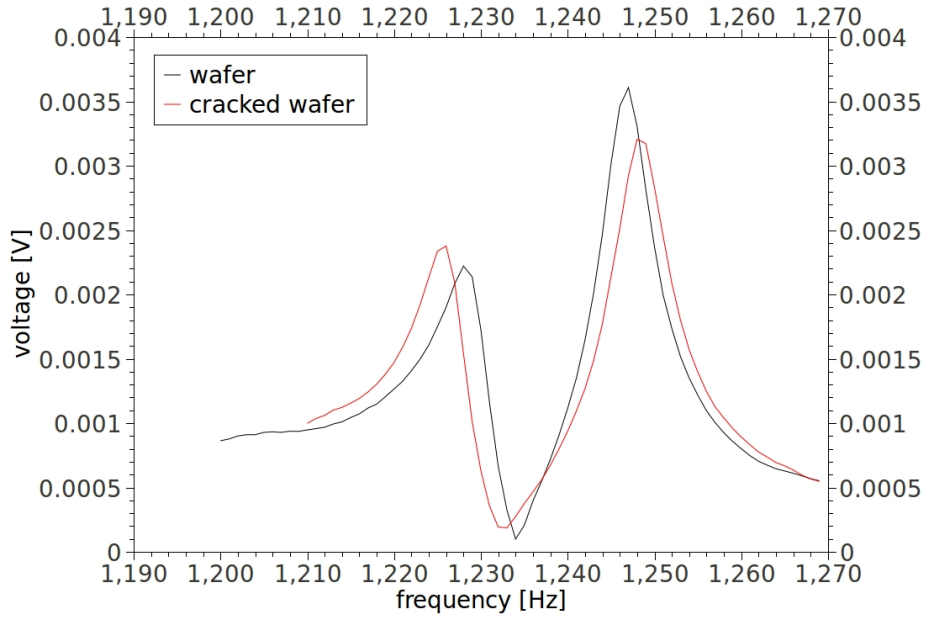


Figure 28: Peak 4, analysed at MP 0.

Impact of the wafer switching process: The measurements with wafer 11 and 12, taken without adding cracks, are used to analyse the possible impacts of the wafer switching process. A variation of two parameters is possible:

- A displacement of the interface between wafer and loudspeaker. This can be an incline of the plastic ring or a displacement of the wafer compared to the loudspeaker.
- A displacement of the wafer compared to the microphone.

The measurements show differences, especially at the fourth analysed oscillation mode. The differences are of the same order of magnitude as those measured with the other wafers. Thus, it can be concluded that the differences in that oscillation mode are mostly caused by those variations.

5.2.2 Signal power at the loudspeaker

The power $P = U \cdot I$ of the signal, measured by ammeter and voltmeter at the loudspeaker, is higher for the cracked wafer, shown in figure 29. The loudspeaker, the connecting rod and the wafer are an oscillating system. To induce oscillations, a specific power is required. The crack is a disruption in the system. The presence of a fatigue crack during vibration reduces the quality factor of the resonance system[4]. Thus a higher power is required to induce oscillations.

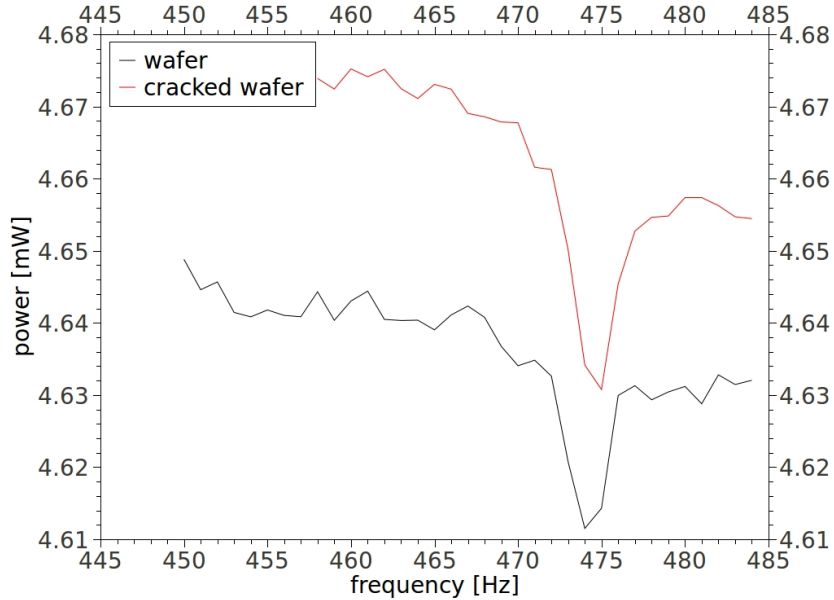


Figure 29: The power P at the loudspeaker, measuring peak 2.

This leads to the possibility of using the loudspeaker as a measurement device. But it can not give information about the position of the cracks.

The power directly at the resonance frequency is lower than the power at lower and higher frequencies. The resonance effect lowers the power needed to induce oscillations in the system. This can only be seen at the first two peaks. The higher peaks describe more complex oscillations with higher curvatures κ_{ij} , $i, j = x, y$. The bending moments M_{kl} , $k, l = x, y$, are proportional to κ_{ij} , as shown in equation (8) and (9).

Therefore, the higher peaks describe oscillations with high bending moments, acting against the deflection. Thus, a high power is needed to induce these oscillations, even at the resonance frequency.

5.2.3 Resonance frequency and wafer mass

The third set of measurements, with one measurement every 0.1 Hz, is taken at MP 0. So, more exact values of the resonance frequencies are obtained to compare the samples. At MP 0 the peaks are all clearly visible. Thus, it was chosen for this set of measurements.

The resonance frequency is linearly dependent on the mass. An example is shown in figure 30. A variation in the dependency may be caused by inhomogeneous thickness and different residual stress levels [3].

Thus, a difference of the wafer mass, caused by the laser cutting process, could lead to a difference in the resonance frequencies. But the mass changes during laser cutting are very small, as shown in table 6. They have almost no impact on the resonance frequency. These impacts are much smaller than the resolution of the experimental setup and were therefore not observed in the measurements.

wafer	mass [g]	mass (cracked) [g]	difference [mg]
1	7.8808	7.8812	0.4
2	7.7857	7.7860	0.3
3	7.8299	7.8303	0.4
4	7.6514	7.6517	0.3
5	7.6939	7.6944	0.5
6	7.8911	7.8910	-0.1
7	7.7737	7.7738	0.1
8	7.8141	7.8141	0
9	7.8061	7.8060	-0.1

Table 6: Wafer mass before and after the laser cutting process.

Possible reasons for the discrepancy are:

- During laser cutting, silicon is vaporized and oxidates again on the interface between air and wafer. In the process some silicon atoms may

not bond to the wafer, but other materials from the air can be added to it.

- Impurities, added to the wafer's surface while handling the samples during the measurements, may cause differences in the wafer mass.

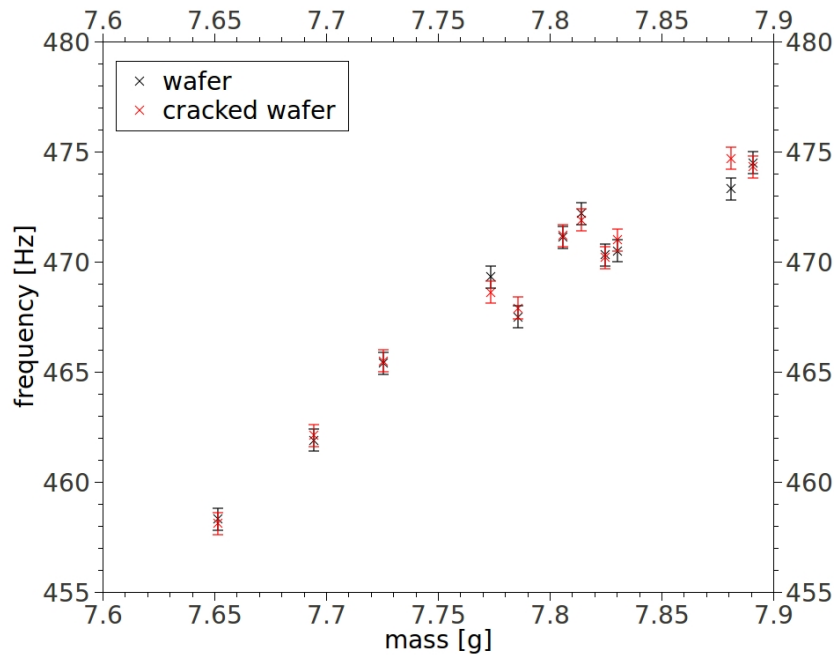


Figure 30: The resonance frequency of peak 2 in dependency of the wafer mass. The red cross marks measurements with the cracked wafers 1-9. The samples 11 and 12 have no added cracks. Thus, for these two samples, the red cross marks a second measurement with the uncracked wafer.

5.3 Variable position

In this chapter the impacts of the cracks on the oscillations at the resonance frequencies are analysed. Because of the measurement errors in $\Delta\Phi$, only the amplitude U_m of the microphone signal is taken.

Because of the strong impacts of small variations in the wafer position at peak 4, the focus is set on the evaluation of the other resonant vibrations.

To compare the oscillation patterns, those of the cracked wafers are subtracted from the corresponding patterns of the unedited wafers. Thus, negative values indicate a stronger oscillation of the cracked wafer, whereas positive values indicate a weaker oscillation.

The maximum of the absolute values of the so gained patterns is taken. In the following, the lower end of the color scale is set to the negative of the maximum. The upper end is set to the positive maximum. Thus, the green area in the middle of the color scale (see figure 18) denotes ≈ 0 . This allows for a better visualization of the differences between the two oscillation patterns. A color shift to red is equivalent to weaker oscillations of the cracked wafer, a color shift to blue equivalent to stronger oscillations.

5.3.1 Impact of the wafer switching process

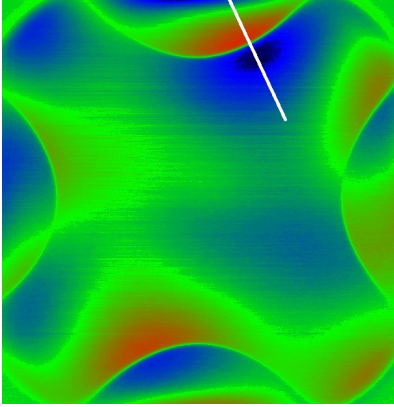


Figure 31: Difference of the oscillation due to a displacement of the wafer's position.

The measurements of wafer 11 and 12 are analysed.

Differences in the oscillation patterns due to a small variation in wafer position can be observed. They are best visible near nodal lines. A change of a nodal line's position does result in the wafer seemingly oscillating stronger on one side of the line, and weaker on the other. If this can be seen on the whole pattern, the reason is not a change of position of the nodal line. In that case, it is a change of position of the wafer between the two measurements. The effect can then be seen on all oscillation patterns.

Figure 31 shows an example of this effect, measured with wafer 11. The white line is parallel to the displacement between the two

measurements, in the frame of reference of the microphone. The effect is strongest at nodal lines normal to the displacement.

The maximal displacement, possible with the experimental setup, is esti-

oscillation mode	minimum [mV]	maximum [mV]
1	-1.04	1.89
2	-1.34	1.16
3	-0.64	1.16
5	-0.46	0.43
6	-0.34	0.34
7	-0.46	0.43

Table 7: Minimal and maximal values of the amplitude differences between the two measurements with wafer 11.

mated to be 1 mm. This estimation is based on the evaluation of the oscillation patterns of the samples 11 and 12. For comparison a measurement was made with an added displacement of (2 mm, 2 mm). It had bigger impacts than those observed in the other measurements.

The measured maximum of the amplitude difference caused by wafer switching is $(10 \pm 5)\%$ of the maximal amplitude of the corresponding oscillation patterns.

5.3.2 Impact of cracks

The measurements of the wafers 1-6 do not yield a systematic difference between the oscillation patterns of wafer and cracked wafer.

The measurements of the wafers 7-9 show impacts of multiple cracks on the amplitude of the oscillations. The cracks result in stronger vibrations of the wafers for the oscillation modes 5-7. Wafer 7 shows the same behaviour for the modes 1-3, whereas wafer 8 and 9 do not. The difference is $(20 \pm 10)\%$ of the maximal amplitude of the corresponding oscillation patterns.

None of the measurements show only local impacts of the cracks on the oscillations. Thus, no information of the position and form of the cracks can be derived.

oscillation mode	minimum [mV]	maximum [mV]
1	-4.06	0.31
2	-4.33	0.34
3	-3.17	0.46
5	-1.34	0.34
6	-1.01	0.15
7	-1.07	0.18

Table 8: Minimal and maximal values of the amplitude differences between wafer 7 and cracked wafer 7.

Some effects causing the amplitude differences were already mentioned:

- the damping of the oscillating system and microslipping at the crack face walls [4]
- different residual stress levels of the wafers [3]
- the stronger power at the loudspeaker
- a variance of the wafer's position relative to the point of excitation

In addition, local differences of E_{Si} and ν_{Si} caused by the cracks have impacts on the oscillations. The density of the cracks and their orientation are the main parameters for these changes[33].

A change of these properties of the whole wafer would result in different resonance frequencies. This can be shown in the FEA of the wafer. It is not consistent with the results of the experiments. Thus, only local changes are possible.

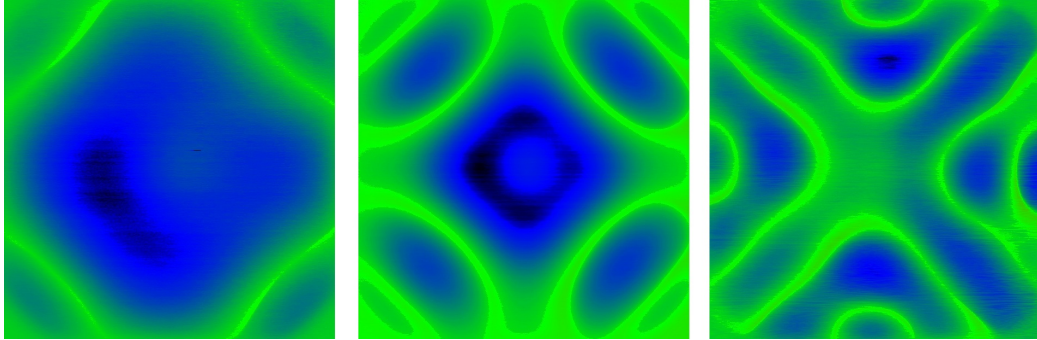


Figure 32: The differences of the resonant oscillations 1, 3 and 5 of wafer 7 are shown. Near the nodal lines, it is approximately 0. In the strongest oscillating areas, it is maximal. In the point of excitation, which is in the center of the wafers, the difference is not 0. This result can be explained by the nature of the measurements with the microphone (see chapter 4.3.3).

5.4 Simulation

The simulation yields many more resonant oscillations than the experiment. In the same frequency range, between 200 Hz and 2700 Hz, over 40 different oscillation patterns are simulated.

Some of those cause the smaller peaks visible in the frequency spectrum (figure 17). But most of them are not measured by the microphone. The resonant vibrations with a big area of the wafer oscillating in the same phase cause the strongest amplitude peaks. This is caused by the measurements with the microphone, as explained in 4.3.3.

peak (experiment)	oscillation pattern (simulation)
1	8
2	12
3	21
4.1, 4.2	23, 24
5	32
6	38
7	49

Table 9: The amplitude peaks, as numbered in this thesis, and the corresponding oscillation patterns from the simulation.

5.4.1 Resonance frequencies

The resonance frequencies vary between experiment and simulation. The simulated resonance frequency is higher than the measured one. This would lead to the conclusion of a systematic error in the simulation, like inaccurate values for E_{Si} and ν_{Si} .

peak	resonance frequency [Hz] experiment	resonance frequency [Hz] simulation	error [%] simulation
1	309.8	310.5	+0.2
2	471.2	488.7	+3.7
3	976.7	1003.7	+2.8
5	1654.9	1599.7	-3.3
6	1996	2039	+2.2
7	2541.5	2692.0	+5.9

Table 10: Resonance frequencies, measured and simulated, at the example of wafer 9.

The values of E_{Si} and ν_{Si} , taken from [30] for the (100) direction, yield the most accurate results. The simulations were repeated with other values, for example the values given by [31] for wave propagation along the 110 crystal direction of a 100 oriented wafer:

$$E_{Si} = 168.96 \cdot 10^9 \text{ Pa}, \quad \nu_{Si} = 0.0625 \quad (70)$$

The exception is oscillation mode 5. It occurs at a lower frequency in the simulation. A reason could not be found.

The smallest error was observed at mode 1, varying between 0.2 % and 1.5 % for different wafers. The biggest error was observed at mode 7, varying between 5.9 % and 6.5 % for different wafers.

Even bigger differences are reached at mode 4 (up to 7.5 %), but due to the differences in the oscillation patterns it is not considered in the evaluation.

The resonance frequencies are linearly dependent on the thickness of the samples. This is equivalent to the linear dependency on the mass shown in the experiment, because the mesh has a homogeneous density.

5.4.2 Viability of the Kirchhoff Plate Theory

The Kirchhoff Plate Theory is accurate for homogeneous, isotropic thin plates. It is not viable for crack inspection of c-Si wafers.

One of the hypotheses of the theory is homogeneity and isotropy of the material. The latter does not apply to c-Si. Implementations of anisotropy into FEM models of elastic plate bending exist, for example [32]. But crack inspection is a more complex problem. Depending on different factors, different values for E_{Si} and ν_{Si} are possible. Examples are the wafer orientation, direction of wave propagation during the oscillation, local impurities or cracks. Kirchhoffs hypotheses, even when expanded to account for anisotropy, do not include those factors. So, another theory has to be chosen for the simulation of crack inspection. The three dimensional elasticity theory considers the different factors.

Furthermore, other methods have to be found to simulate the problem, because "the method [FEA] is poorly adapted to a solution of the so-called singular problems, e.g. plates and shells with cracks"[15].

6 Conclusion

Measurements with several monocrystalline silicon wafers have been made in the frequency range between 200 Hz and 2.7 kHz. The resonance frequencies have been identified and 6 corresponding oscillation patterns have been measured. Afterwards, cracks were introduced to the wafers with a laser scribing machine. The measurements have been repeated and the results compared. The resonance frequencies and the wafer's mass are not changed by adding cracks.

The power at the loudspeaker is higher when the oscillations of the cracked wafers are induced. The difference can only be observed on the wafers with multiple added cracks and is of the magnitude of $\approx 1\%$. Thus, using the loudspeaker as a measurement device is possible.

The deflection of the plate shows small variations between the unedited and the once cracked wafers. The measurements of those wafers do not yield a systematic difference of the oscillation patterns. The biggest disturbance is the impact of small variations of the wafer position in the measurement setup, caused by the wafer switching process. Therefore, future experiments should further reduce these variations.

The wafers with multiple added cracks show stronger oscillations at higher resonance frequencies. The reasons for this effect include the higher power at the loudspeaker and local variations of E_{Si} and ν_{Si} of the samples caused by the cracks. These variations are dependent on the orientation and the density of the cracks. But no local differences of the oscillation patterns could be tied to the position of the added cracks.

A finite element analysis of the wafer oscillation has been made. It yields the same oscillations and resonance frequencies with a maximal error of 6.5%. But the underlying theory, the Kirchhoff Plate Theory, does not account for anisotropy and local differences, for example due to cracks. Thus, it is not viable for simulating the impacts of cracks on the oscillations. Furthermore, the finite element method is poorly adapted to the problem of plates with cracks. Thus another method for simulating the problem has to be used.

References

- [1] European Photovoltaic Industry Association.
Global Market Outlook 2016.
May 2012.
- [2] European Photovoltaic Industry Association.
Solar Generation 6.
February 2011.
- [3] S.R. Best, D.P. Hess, A. Belyaev, S. Ostapenko, J.P. Kalejs.
Audible vibration diagnostics of thermo-elastic residual stress in multi-crystalline silicon wafers.
Applied Acoustics (2006), Volume 67, Issue 6, p. 541–549.
- [4] B. Wincheski, M. Namkung, J.P. Fulton.
Quality Factor and Microslipping of Fatigue Cracks in Thin Plates at Resonant Vibration.
IEEE Ultrasonic Symposium, October 1992.
- [5] H. J. Hovel.
Semiconductors and Semimetals - Volume 11: Solar Cells.
Academic Press Inc., New York 1975.
- [6] Applied Materials.
Advanced wire sawing technology for solar photovoltaic cells.
http://www.appliedmaterials.com/sites/default/files/Advanced-Wire-Sawing-Technology-Whitepaper_en.pdf, retrieved on the 17.1.2013.
- [7] T. Behm, W. Fütterer, C. Funke, S. Kaminski, H.-J. Möller, R. Rietzschel, T. Wagner.
Challenges of the wire saw wafering process.
Photovoltaics International (2011), Ed. 11, p. 36-47.
- [8] C.A. Felippa.
Kirchhoff Plates: Field Equations
Lecture notes for *Advanced Finite Element Methods for Solids, Plates and Shells*, University of Colorado at Boulder.
<http://www.colorado.edu/engineering/CAS/courses.d/AFEM.d/AFEM.Ch20.d/AFEM.Ch26.pdf>, retrieved on the 3.2.2012.
- [9] E.J. Ruggiero.
Modeling and Control of SPIDER Satellite Components.

- Dissertation, Virginia Polytechnic Institute and State University. Blacksburg, Virginia, 2005.
- [10] C. Kittel.
Introduction to Solid State Physics, 8th Edition.
John Wiley & Sons, 2004.
 - [11] E.F.F. Chladni.
Entdeckungen über die Theorie des Klanges.
Breitkopf und Härtel, Leipzig 1787.
 - [12] M. Faraday.
On a Peculiar Class of Acoustical Figures; and on Certain Forms Assumed by Groups of Particles upon Vibrating Elastic Surfaces.
Phil. Trans. Royal Society London (1831), vol. 121, p.229-340.
 - [13] M. Nikkhah-Bahrami, M. Loghmani, M. Pooyanfar.
Analytical Solution for Free Vibrations Rectangular Kirchhoff Plate from Wave Approach
Proceedings of World Academy of Science: Engineering & Technology (2008), vol. 41, p.221.
 - [14] J.R. Looker, J.E. Sader.
Flexural Resonant Frequencies of Thin Rectangular Cantilever Plates.
J. of Applied Mechanics, vol. 75, issue 1, 2008, p. 011007.
 - [15] E. Ventsel, T. Krauthammer.
Thin plates and shells - Theory, analysis and applications
Marcel Dekker, Inc., New York / Basel 2001.
 - [16] CSC - IT Center for Science, Espoo.
Official homepage of the Elmer software.
<http://www.csc.fi/english/pages/elmer>, retrieved on the 14.2.2013.
 - [17] M.J. Turner.
The direct stiffness method of structural analysis.
Structural and Materials Panel Paper, AGARD Meeting, Aachen, 1959.
 - [18] C.A. Felippa.
Lecture notes for *Introduction to Finite Element Methods*, University of Colorado at Boulder.
<http://www.colorado.edu/engineering/CAS/courses.d/IFEM.d/Home.html>,
retrieved on the 5.2.2013.

- [19] M.J. Turner, R.W. Clough, H.C. Martin, L.J. Topp.
Stiffness and deflection analysis of complex structures.
J. of the Aeronautical Sciences, vol. 23, 1956, p. 805–824.
- [20] H.Mang, G.Hofstetter.
Festigkeitslehre.
Springer, Wien / New York 2000.
- [21] B.M. Irons.
A frontal solution scheme for finite element analysis.
Int. J. of Numerical Methods in Engineering, vol. 2, 1970. p. 5-32.
- [22] I.S. Duff, J.K.Reid.
The Multifrontal Solution of Indefinite Sparse Symmetric Linear Equations.
ACM Transactions on Mathematical Software, vol. 9, issue 3, 1983, p. 302-325.
- [23] Agilent Technologies.
Agilent 33220A 20 MHz Function/Arbitrary Waveform Generator - Data Sheet.
March 2005.
- [24] Agilent Technologies.
Agilent 34401A 6 1/2 Digit Multimeter - User's Guide.
August 2007.
- [25] Fluke.
Fluke 45 Dual Display Multimeter - Users Manual.
July 1997.
- [26] Stanford Research Systems.
Model SR530 Lock-In Amplifier.
August 2001.
- [27] LEM Technologies.
Cellule Microphone EM100T.
March 1997.
- [28] B. Berkovski, T. Markvart.
Solar Electricity.
John Wiley & Sons, Chichester 1994.

- [29] T.A.Davis.
Official homepage of UMFPACK.
<http://www.cise.ufl.edu/research/sparse/umfpack/>, retrieved on the 10.2.2013.
- [30] M.A. Hopcroft, W.D. Nix, T.W. Kenny.
What is the Young's Modulus of Silicon?
 J. of Microelectromechanical Systems, vol. 19, no. 2, 2010, p. 229-238.
- [31] M. Pander.
Mechanische Untersuchungen an Solarzellen in PV-Modulen mittels Finite – Elemente – Modellierung.
 Master thesis, Hochschule für Technik, Wirtschaft und Kultur. Leipzig, 2009.
- [32] N. Nataraj, P.K. Bhattacharyya.
On a mixed-hybrid finite element method for anisotropic plate bending problems.
 Int. J. for Numerical Methods in Engineering, vol. 39, 1996, 4063-4089.
- [33] S. Giordano, L. Colombo.
Effects of the Orientational Distribution of Cracks in Solids.
 Phys. Review Letters, vol. 03, 2007; 98(5):055503.

Ich habe mich bemüht, sämtliche Inhaber der Bildrechte ausfindig zu machen und ihre Zustimmung zur Verwendung der Bilder in dieser Arbeit eingeholt. Sollte dennoch eine Urheberrechtsverletzung bekannt werden, ersuche ich um Meldung bei mir.

A Appendix

A.1 Symbols

<i>Symbol</i>	<i>Description</i>	<i>Unit</i>
A	normalized area in equation (18)	m^2
A_w	ground area of the wafer	m^2
a	length of the plate	m
b	width of the plate	m
h	thickness of the plate	m
\vec{b}	volume forces or distributed load	Nm^{-3}
\mathbf{B}	strain-displacement matrix	m^{-1}
\mathbf{C}	elastic modulus	Nm^{-2}
C_{ijkl}	elastic modulus components	Nm^{-2}
C_{ij}	elastic modulus components (Voigt notation), $i, j = 1, 2, 3$	Nm^{-2}
E	elastic modulus of an isotropic material	Nm^{-2}
\vec{d}	nodal displacements	m
d_{ij}	nodal displacement components, $i = x, y, z; j = 1, 2, \dots, n_e$	m
D_{ij}	flexural rigidity components, $i, j = 1, 2, 3$	Nm
D	flexural rigidity of an isotropic plate	Nm
\vec{e}	2-dimensional strain	—
e_{ij}	strain components, $i, j = x, y, z$	—
E_{int}	internal energy / elastic strain energy	Nm
E_{kin}	kinetic energy	Nm
E_{pot}	potential energy	Nm
\vec{F}	nodal forces	N
f_{ij}	nodal force components, $i = x, y, z; j = 1, 2, \dots, n_e$	N
h_w	thickness of a wafer	m
I	current measured by the ammeter	A
k_i	wave numbers, $i = 1, 2$	m^{-1}
L	Lagrangian	Nm
M_{ij}	bending moment, $i, j = x, y$	N
m_w	mass of a wafer	kg
m	number of elements in the system	—
n_e	number of nodes per element	—
n_s	number of nodes in the system	—

\mathbf{N}	shape function matrix	—
N_i	shape functions, $i = 1, 2, \dots, n$	—
\mathbf{P}	3×3 matrix in equation (43)	m^{-1}
P	power	W
p_s	sound pressure	Nm^{-2}
q	force per unit area in direction of the z-axis	Nm^{-2}
Q_i	transverse shear force, $i = x, y$	Nm^{-1}
r_m	distance between a point of the wafer and the microphone	m
\mathbf{S}	stiffness matrix	Nm^{-1}
\mathbf{T}_f	force transformation matrix	—
\mathbf{T}_d, \mathbf{T}	displacement transformation matrix	—
\vec{u}	deflection of the plate, with components (u, v, w)	m
U	voltage measured by the voltmeter	V
U_{DC}	DC voltage tuned at the FG	V
U_m	amplitude of the microphone's signal	V
U_s	signed amplitude	V
V	potential	Nm
w_i	functions of x and t in equation (26)	—
w_m	displacement of the speaker's membrane	m
x_0, y_0	arbitrary constants in equation (22)	—
$\bar{x}, \bar{y}, \bar{z}$	components of the element CS $(\bar{x}, \bar{y}, \bar{z})$	m
Γ°	boundary of an element	m
κ_{ij}	curvatures of the midplane, $i, j = x, y$	m^{-1}
ν	Poisson ratio	—
Π	total potential energy funcional	Nm
ρ	density	kg m^{-3}
$\vec{\sigma}$	2-dimensional stress	Nm^{-2}
σ_{ij}	stress components, $i, j = x, y, z$	Nm^{-2}
φ	angle between components of element CS and global CS	rad
c	$\cos \varphi$	—
s	$\sin \varphi$	—
Φ	arbitrary function in equation (21)	—
ϕ_m	phase of the microphone signal	—
ϕ_g	phase of the generated signal by the FG	—
$\Delta\phi$	phase difference between ϕ_m and ϕ_g	—
ω	angular frequency	s^{-1}
Ω°	ground area of an element	m^2
—	denotes values in the element CS (chapter 3.2.6)	—
o	denotes values of single elements (chapter 3.2.6)	—

A.2 Constants and material properties

<i>Symbol</i>	<i>Description</i>	<i>Value</i>	<i>Source</i>
ρ_{Si}	density of crystalline silicon	2328 kg m^{-3}	[28]
E_{Si}	elastic modulus of crystalline silicon	$1.3 \cdot 10^{11} \text{ Nm}^{-2}$	[30]
ν_{Si}	Poisson ratio of crystalline silicon	0.28	[30]

Note that the values given here are the ones used in this thesis. Some, like E_{Si} , are more complex because of anisotropy.

A.3 Abbreviations

c-Si:	crystalline silicon
FEA:	finite element analysis
DSM:	direct stiffness method
CS:	coordinate system
FG:	function generator
LIA:	lock-in amplifier
ADC:	analog-to-digital converter
DSO:	digital storage oscilloscope
AC:	alternating current
DC:	direct current
VTK:	visualization toolkit
MP:	measurement point

A.4 Mesh for the wafer

```
**** ElmerGrid input file for structured grid generation ****
Version = 210903
Coordinate System = Cartesian 2D
Subcell Divisions in 2D = 3 3
Subcell Limits 1 = 0 0.0604 0.0646 0.125
Subcell Limits 2 = 0 0.0425 0.0453 0.087
Material Structure in 2D
1 1 1
1 2 1
1 1 1
End
Geometry Mappings
! mode   line   limits(2)   Np       params(Np)
1       3      0.0424      0.0826    8   0 0 0.019 0.019 0.106 0.019 0.125 0
1       0      0.0212      0.045     8   0 0 0.019 -0.019 0.106 -0.019 0.125 0
End
Materials Interval = 1 1
Boundary Definitions
! type   out   int   double   of the boundaries
1       2     1
2       0     1
End
Numbering = Horizontal
Element Degree = 1
Element Innernodes = False
Triangles = True
Surface Elements = 10000
Element Densities 1 = 1 0.8 1
```

Figure 33: The file for the wafer mesh, created with ElmerGrid[16].

A.5 Table of figures

<i>Figure</i>	<i>Description</i>	<i>Wafer</i>	<i>Page</i>
1	impacts of the sawing process		4
2	definition of the midplane		6
3	bending stresses and moments		9
4	wafer mesh		14
5	force transformation		20
6	schematic setup		24
7	experimental setup		25
8	reading points on the samples		31
9	fracture area of a wafer		33
10	wafer 2	2	34
11	wafer 3	3	34
12	wafer 5	5	34
13	wafer 6	6	35
14	wafer 7	7	35
15	wafer 8	8	35
16	wafer 9	9	35
17	enumeration of the peaks	1	38
18	color scale		39
19	correction of the phase difference	7	40
20	measurement errors	7	41
21	resonant oscillation 1	7	42
22	resonant oscillation 2	7	43
23	resonant oscillation 3	7	43
24	resonant oscillation 4	9	44
25	resonant oscillation 5	7	45
26	resonant oscillation 6	7	45
27	resonant oscillation 7	7	45
28	amplitude peak 4	4	47
29	power at the loudspeaker	6	48
30	resonance frequencies of oscillation 2	1-12	50
31	difference of the oscillation pattern 2	11	51
32	differences of the oscillation patterns 1,3 and 5	7	53
33	mesh for the wafer		64

B Curriculum Vitae

name: Stefan Mitterhofer
date of birth: May 3rd 1987
place of birth: Meran, Italy

master thesis: An acoustic setup for vibration analysis
of silicon wafers

2006 - present: diploma and master studies in physics
Faculty of Physics, University of Vienna
2006: school leaving examination (Matura)
2001 - 2006: high school
Realgymnasium Albert Einstein, Meran
1998 - 2001: middle school
Mittelschule Peter Mitterhofer, Partschins
1993 - 1998: primary school
Grundschule Peter Mitterhofer, Partschins

C Abstract - english

An acoustic setup for vibration analysis of silicon wafers

An exponential growth in the installed capacity of photovoltaic power plants has been observed in the last few years. The technology is predicted to become more cost-effective and competitive in the coming years. Therefore a further growth is expected.

Crystalline silicon is the most common photovoltaic technology with about 80 % of today's market share. Different stages of the manufacturing process are one source of microcracks and impurities in the wafers. Systems for quality control, which can be introduced into the manufacturing process, are therefore increasingly demanded.

This master thesis investigates the impacts of the wafer's surface cracks on its resonance frequencies and vibrations in an acoustic setup. A loudspeaker is used to induce oscillations in the wafers. The sound waves caused by these oscillations are measured with a microphone.

Mathematically the wafers can be seen as thin plates, described by the Kirchhoff Plate Theory. With finite element analysis the different oscillations are modelled and compared to the experimental results.

The measurements show no systematic impacts of single cracks on the oscillations. Multiple cracks yield stronger oscillations of the samples, especially at higher frequencies. The main reason are local differences of the physical properties of the material near the cracks, depending on their density and orientation. A higher power at the loudspeaker can be measured when inducing oscillations in the cracked wafers. Thus, it can be used as a measurement device.

It is shown, that the Kirchhoff Plate Theory is not viable for crack inspection of the wafers, because it does not account for local variations of the physical properties.

D Abstract - german

Eine akustische Messanordnung zur Untersuchung resonanter Schwingungen von Silizium-Wafern

In den letzten Jahren stieg die installierte Kapazität der Photovoltaikanlagen exponentiell an. Die Technologie wird voraussichtlich in den nächsten Jahren kosteneffizienter und marktfähiger. Daher wird ein weiterer Anstieg erwartet. Kristallines Silizium ist mit 80 % Marktanteil die vorrangige Technologie bei Photovoltaikanlagen. Verschiedene Stufen im Herstellungsprozess der Wafer können zu mechanischen Defekten und Fehlstellen führen. Deshalb sind Methoden zur Qualitätssicherung zunehmend gefragt, welche in den Herstellungsprozess integriert werden können.

Diese Masterarbeit untersucht die Einflüsse von Sprüngen in der Oberfläche der Wafer auf ihre Resonanzfrequenzen und resonanten Schwingungen mithilfe einer akustischen Messanordnung. Ein Lautsprecher wird zum Anregen der Oszillationen verwendet. Die dadurch verursachten Schallwellen werden mit einem Mikrofon gemessen.

Das mathematische Modell der Wafer sind dünne Platten, beschrieben von der Kirchhoff Plate Theory. Mithilfe der Finite-Element-Analyse werden die verschiedenen Schwingungen simuliert und mit den experimentellen Ergebnissen verglichen.

Einzelne Sprünge ergeben keinen systematischen Einfluss auf die Messungen. Mehrere Sprünge führen zu stärkeren Schwingungen der Wafer, vor allem bei höheren Frequenzen. Der Grund liegt vor allem in Unterschieden der physikalischen Eigenschaften von Silizium in der Nähe der Fehlstellen, abhängig von deren Dichte und Anordnung. Weiters wurde eine höhere Leistung am Lautsprecher gemessen, während die bearbeiteten Wafer zum Schwingen angeregt wurden. Dies ermöglicht es, ihn als Messgerät zu verwenden.

Die Kirchhoff Plate Theory ist nicht geeignet für die Untersuchung von Fehlstellen in den Wafern, da sie die lokalen Unterschiede nicht mit einbezieht.